Fall 10-25-2018

Crustal Seismic Anisotropy of the Ruby Mountains Core Complex and Surrounding Northern Basin and Range

Justin T. Wilgus

Recommended Citation

Wilgus, Justin T.. "Crustal Seismic Anisotropy of the Ruby Mountains Core Complex and Surrounding Northern Basin and Range." (2018). https://digitalrepository.unm.edu/eps_etds/250

Justin T. Wilgus
Candidate

Earth and Planetary Sciences
Department

This thesis is approved, and it is acceptable in quality and form for publication:

Approved by the Thesis Committee:

Dr. Brandon Schmandt, Chairperson

Dr. Karl Karlstrom

Dr. Lindsay Lowe Worthington

CRUSTAL SEISMIC ANISOTROPY OF THE RUBY MOUNTAINS CORE COMPLEX AND SURROUNDING NORTHERN BASIN AND RANGE

by

JUSTIN T. WILGUS

B.S. IN GEOLOGY, MINOR IN MATHEMATICS
NORTHERN ARIZONA UNIVERSITY, 2015

THESIS

Submitted in Partial Fulfillment of the
Requirements for the Degree of

Master of Science
Earth and Planetary Sciences

The University of New Mexico
Albuquerque, New Mexico

December, 2018

ACKNOWLEDGEMENTS

I would like to thank my advisor Brandon for giving me this opportunity and always motivating my progress. I am indebted to the seismology group at UNM particularly Chengxin Jiang, Han Zhang, and Margaret Glasgow for their constant willingness to impart conceptual knowledge and discuss science with rigor. To my family and friends, you have experienced this journey first hand and have trudged with me on this road of happy destiny supporting me throughout, thank you. Finally, I would like to thank my wonderful wife Kelly for being the best teammate a man can ask for.

Crustal Seismic Anisotropy of the Ruby Mountains Core Complex and Surrounding Northern Basin and Range

Justin T. Wilgus

B.S. in Geology, Minor in Mathematics, Northern Arizona University, 2015

M.S. in Earth and Planetary Science, University of New Mexico, 2018

ABSTRACT

Metamorphic core complexes (MCC) are distinctive uplifts that expose deeply exhumed and deformed crustal rocks due to localized extensional deformation. Consequently, their detailed structure provide a window into deep crustal mechanics. The North American Cordillera contains numerous MCC, one of which is the Ruby Mountains core complex (RMCC) located in the highly extended northern Basin and Range. To constrain the extent to which anisotropy below the RMCC deviates from the regional Basin and Range average and test the depth dependence of crustal anisotropy we conduct a radial anisotropy investigation below the RMCC and surrounding northern Basin and Range. Data from the Ruby Mountains Seismic Experiment (RMSE) and surrounding networks are used to cross correlate ambient noise and obtain Rayleigh and Love wave signals. Using the frequency-time analysis (FTAN) method we compute inter-station Rayleigh and Love wave dispersion curves and invert for phase velocity maps for periods 5-40 s. A Bayesian Markov chain Monte Carlo (BMMC) inversion technique is used to obtain 3D Vs structure and estimate radial anisotropy as a function of depth and geographic location. Results show a relatively simple but pervasive, ~6%, positive ($V_{SH} > V_{SV}$) signal distributed throughout the middle crust (~5-20 km) of the study region required at 95% confidence. In contrast, there is an absence of similarly strong and significant lower crustal radial anisotropy. Interestingly, the volume directly below the RMCC does not uniformly deviate from the regional trend. Middle crustal radial anisotropy is stronger than average beneath the southern RMCC and weaker than the regional average beneath the northern RMCC. The lack of clear correlation between the RMCC and radial anisotropy in the crust suggests mechanisms of core complex exhumation either never produced a resolvable radial anisotropy pattern or that anisotropy associated with RMCC exhumation has subsequently been overprinted. Multiple mechanisms have the potential to explain the regional depth distribution of anisotropy, including decreasing prevalence of mica from the middle-to-lower crust and a temperature-controlled rheological transition from localized ductile deformation in the middle crust to distributed ductile deformation in the lower crust.

TABLE OF CONTENTS

LIST OF FIGURES

LIST OF TABLES

LIST OF EQUATIONS

1 INTRODUCTION

The Basin and Range is a physiographic province located on the western edge of the North American plate that formed as a result of extensional tectonics (Fig. 1).

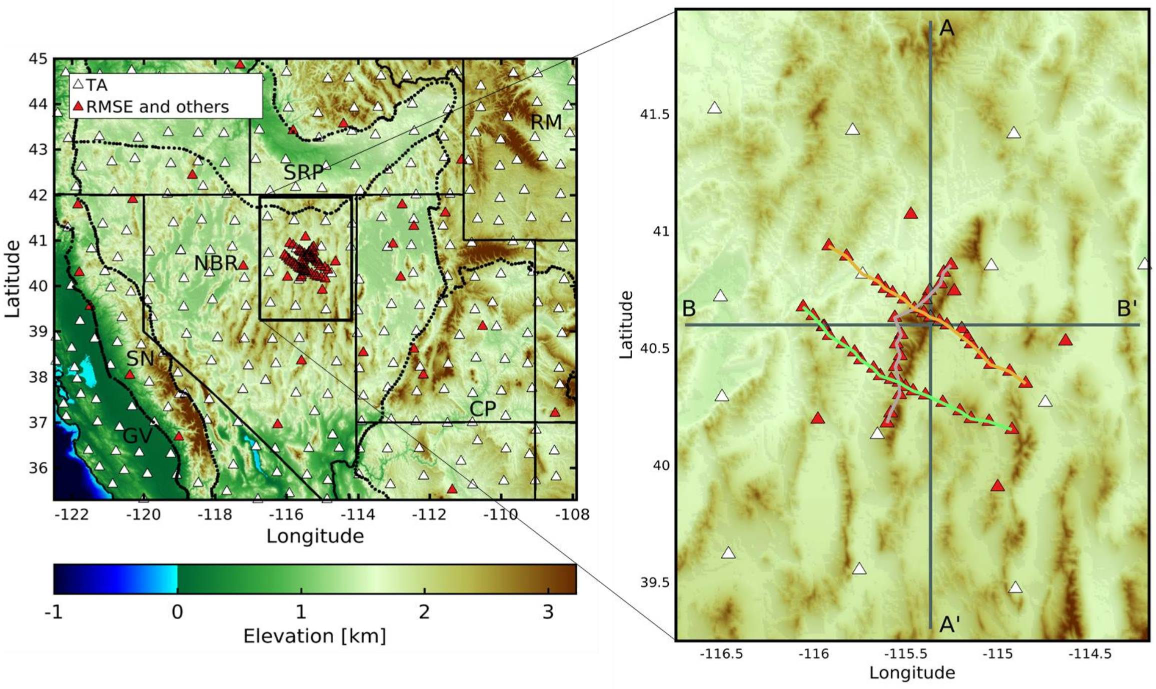

Figure 1. A) Large area topography. Stations used for ambient noise cross correlations (red) and Transportable Array (TA) stations (white) used in USANT model. Dotted lines define geologic provinces from Fenneman, (1917): Colorado Plateau (CP), Great Valley (GV), northern Basin and Range (NBR), Rocky Mountains (RM), Sierra Nevada (SN), Snake River Plain (SRP). B) Focus of study area showing local topography and RMSE configuration. Colored lines show cross sections used in this study.

Distributed throughout Basin and Range are several distinctive extensional uplifts that, relative to the Basin and Range, record an anomalously high degree of localized strain. These structures expose deeply exhumed and deformed crustal rocks and are known as metamorphic core complexes (MCC) (Fig. 2). The Ruby Mountains core complex (RMCC) is located in the central portion of the northern Basin and range (Fig. 2). MCC exhumation mechanisms are debated but include extension rate driven

(Buck, 1988; Lavier et al., 1999) and lateral pressure gradient driven models (Block and Royden, 1990).

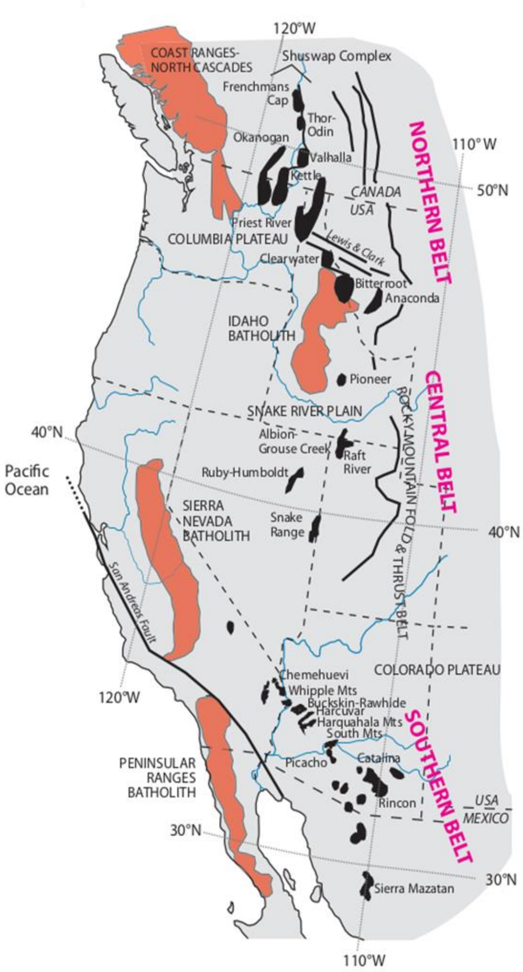

Figure 2. Distribution (black blobs) of MCC throughout the Basin and Range and North American Cordillera from Whitney et al., (2013).

Anisotropy is simply the property of being directionally dependent. Seismic anisotropy refers to wave speed dependence on propagation direction (azimuthal anisotropy) or polarization direction (radial anisotropy). Development of seismic anisotropy in the lithosphere can provide insight into deep subsurface deformation. The first seismological inquiries into anisotropy and its geological implications began as the theory of plate tectonics was being developed (Backus 1962; Hess, 1964). Measurement of seismic anisotropy has since evolved into an important observable that can provide insight into past and present deformation processes in the crust and mantle (Lin et al., 2011; Lin et al., 2016; Long and Becker, 2010; Long and Silver, 2008; Moschetti et al., 2010; Porter et al., 2011; Shapiro et al., 2004). Seismic anisotropy is prevalent within the Earth and is considered more of a rule rather than an exception (Babuska and Cara, 1991). Strong anisotropy is observed in the lithosphere where deformation is likely more concentrated than in most of the mid-mantle (Long and Becker, 2010). As seismic data resources and computational methods improve local crustal anisotropy studies using surface waves derived from ambient noise are increasingly common (Das and Rai, 2017; Dreiling et al., 2017; Fu and Li, 2015; Jaxybulatov et al., 2014; Jiang et al., 2018; Lynner et al., 2018; Ojo et al., 2017; Xie et al., 2013; Xie et al., 2017). Measurements from these types of studies are providing new perspectives on structure and deformation in tectonically complex regions of the crust.

To first order the source of seismic anisotropy within the mantle is generally accepted to be lattice preferred orientation of olivine, which is the most prevalent mineral in the mantle. However, olivine is not a major constituent of continental crust (Nesbitt and Young, 1984) and anisotropy in the crust and upper mantle may be uncorrelated as demonstrated by depth-dependent variations in anisotropy beneath the western U.S. (Lin et al., 2011). Although crustal seismic anisotropy investigations are becoming increasingly common, the relative importance of potential controls on crustal seismic anisotropy remains enigmatic (Erdman et al., 2013; Hacker et al., 2014; Mainprice and Nicolas, 2013; Ward et al., 2012; Xie et al., 2015) leading to complexities in interpretation of constraints on crustal seismic anisotropy. Previous regional studies of the western US found strong radial and azimuthal anisotropy in the Basin and Range crust, which may be related to the hot regional geotherm (Hasterok and Chapman, 2007) and deep crustal flow (Moschetti et al., 2010; Lin et al., 2011; Xie et al., 2015).

From 2010 to 2012 a 50-station array of three component broadband seismometers, known as the Ruby Mountains Seismic Experiment (RMSE) was deployed over the RMCC (Fig. 1) (Litherland and Klemperer, 2017). We jointly analyze inter-station Rayleigh and Love wave dispersion curves derived from ambient noise interferometry using the RMSE and surrounding stations and a previous study using Transportable Array (TA) data (USANT; Ekström, 2014). These dispersion curves are inverted for phase velocity maps which serve as the basis for a Bayesian Markov chain Monte Carlo (BMMC) inversion for Vs structure and anisotropy. This relatively new method of inversion (Shen et al., 2012) allows for statistical quantification and determination of where anisotropy is needed horizontally and at depth. Further motivation for this study comes from initial isotropic inversions which showed that isotropic Vs models can rarely fit Rayleigh and Love wave dispersion measurements within their uncertainties. Conversely, anisotropic inversions for Vs structure are found to explain both types of measurements well.

No detailed seismic anisotropy investigations using surface waves have been conducted on a local scale at a MCC. The tectonic setting of the region, the localized strain associated with exhumation of the RMCC, and the availability of dense broadband data from the RMSE and the TA provide an ideal opportunity to statistically quantify seismic anisotropy as a function of depth beneath RMCC and surrounding northern Basin and Range (NBR). Based on previous regional crustal anisotropy studies (Lin et al., 2011; Moschetti et al., 2010), MCC exhumation modelling (Block and Royden, 1990; Buck, 1988; Lavier et al., 1999; Rey et al, 2009), and the relative degree of localized strain associated with the RMCC we might expect to see a unique pattern of anisotropy below the RMCC and a relatively uniform horizontally fast pattern of anisotropy in the deep crust of the NBR surrounding the RMCC.

2 BACKGROUND

2.1 Tectonic setting

As suggested in its topographically derived name the Basin and Range is characterized by a roughly parallel sequence of nearly N-S trending mountain ranges with intervening basins. The geologic history of the Basin and Range helps define its modern distinctive physiographic features. Formation of the Basin and Range began in the Paleogene following cessation of crustal shortening along much of the North American Cordillera during the Sevier and Laramide orogenic events. Western plate boundary re-organization including subduction of the Kula-Farallon ridge in the north and the Pacific-Farallon ridge in the south led to decreased subduction zone width and coincided with a transition from dominantly compressional to dominantly extensional deformation in the Cordilleran interior (Schellart et al., 2010). Diminished compressional stress and thick elevated continental crust gave rise to gravitational collapse in what became the Basin and Range (Coney, 1987) with some extensional deformation exploiting fault zones that previously accommodated compressional stress (Coney and Harms, 1984). The beginning of Columbia River flood basalt volcanism in the Miocene (~17 Ma) was coeval with continued growth of the San Andreas transform plate boundary and accelerated the rate of extension in the Basin and Range (Camp et al., 2015). Today, Basin and Range extension continues at a more subdued rate as the San Andreas transform margin grows at the expense of the ~1000 km wide Juan de Fuca subduction zone.

Reconstruction of balanced cross-sections indicates that the NBR has undergone up to ~100% Cenozoic lithospheric extension (Hamilton and Myers, 1966; Wernicke et al., 1982). Furthermore, smaller individual domains may have experienced up to 300% extension (Gans, 1987). This extension thinned a high elevation orogenic plateau known as the Nevadaplano (Coney and Harms, 1984; DeCelles, 2004; Zandt et al., 1995) which formed contemporaneous with the Sevier orogeny during the Cretaceous and Paleogene.

Currently, the majority of deformation in the NBR, the focus region of this study, occurs at its western (~10 mm/yr transtension) and eastern (~3-4 mm/yr extension) flanks (Hammond and Thatcher, 2004). The central portion of the NBR is currently undergoing widespread distributed extension of 0.6 mm/yr (Hammond, 2014). Accommodation for this extension occurs on an extensive network of mainly normal faults within mostly half graben structures (Wernicke, 1981). The Moho below the Basin and Range is generally flat (Klemperer et al., 1986) with depths varying between 25 - 35 km (Schmandt et al., 2015; Zandt et al., 1995). Relative to the cratonic interior of North

America the Basin and Range lithosphere is thin with lithosphere asthenosphere boundary (LAB) depths ranging between ~60 - 85 km (Hansen et. al, 2015; Levander and Miller, 2012). Heat flow is high with a NBR median value of 79 mW/m^2, which could enable ductile deformation at relatively shallow depths compared to other regions of the western U.S. crust (Hasterok and Chapman, 2007).

2.2 Metamorphic core complexes

The magnitude of extension within the Basin and Range has been so great that in many localities deep, middle to lower, crustal rocks have been exhumed to the surface (Hodges and Walker, 1990; Hudec, 1992; Miller et al., 1999, Platt et al., 2015). These exhumed terranes are called metamorphic core complexes (MCC) and are characterized by anomalously deformed and metamorphosed rock (Davis and Coney, 1979). The general structure of MCC consists of: (1) a deep crust derived metamorphic core; (2) a detachment consisting of cataclasites in the immediate vicinity and mylonites in the periphery; and (3) an unmetamorphosed normally faulted detachment hanging wall (Platt et al., 2015) (Fig. 3).

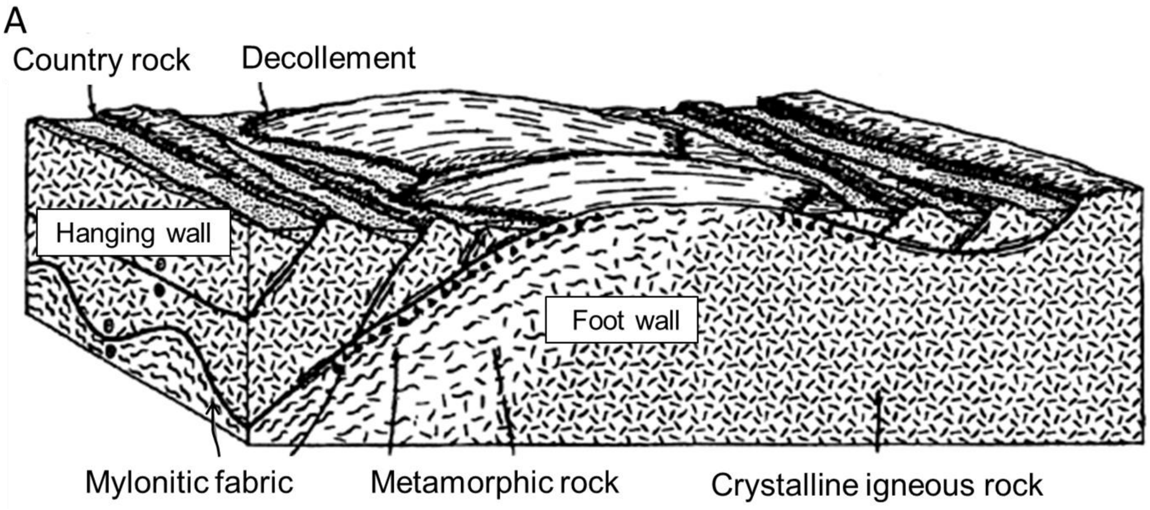

Figure 3. Idealized schematic of a metamorphic core complex, modified after Spencer and Reynolds, (1989).

Although North America Cordillera MCC have variable exhumation histories many are polygenetic (Coney and Harms, 1984), originally forming during Mesozoic compression, concurrently with Nevadaplano development, followed by a second overprinting deformation event during Cenozoic extension (McGrew et al., 2000) and Nevadaplano collapse. However, the role of Cenozoic deformation in North American Cordillera MCC generally diminishes north of latitude 50° (Armstrong, 1982). MCC occur along the entire North American Cordillera (Fig. 2) and there are three within the NBR, one of which is the RMCC (Fig. 2).

2.3 Ruby mountains metamorphic core complex

Exhumation of the RMCC was accommodated in the brittle and ductile deformation regimes. The earliest known RMCC exhumation in the brittle or fault-controlled regime was contemporaneous with the initiation of Basin and Range extension ~16-17 Ma (Colgan et al., 2010) and the latest pulse of deformation in the brittle regime occurred between 10-13 Ma (Colgan et al., 2010; Haines and van der Pluijm, 2010). Brittle deformation continues on nearby faults at a slower rate today, as constrained by geodetic measurements and seismicity (e.g., Hammond and Thatcher, 2007; Herrmann et al., 2011). However, the bulk of RMCC exhumation, or the main phase, occurred by deep crustal deformation in the ductile regime between the Oligocene and early Miocene, ~20-29 Ma (Dokka et al., 1986; Sullivan and Snoke, 2007) before widespread extension in the Miocene formed the Basin and Range. Therefore, the RMCC records a prolonged history of exhumation (Sullivan and Snoke, 2007) making it a prime example of a polygenetic MCC.

During the Mesozoic numerous magmatic, metamorphic, and deformational events affected the rocks of the RMCC (Sullivan and Snoke, 2007). Well preserved Mesozoic compressional deformational structures and fabrics affect and overprint rocks below the mylonitic shear zone (Hudec, 1992; MacCready et al., 1997; Mcgrew, 2000). Peak metamorphic conditions occurred in the late Cretaceous (Sullivan and Snoke, 2007). Immediately following cessation of compression in the late Cretaceous the RMCC was subjected to extension (Sullivan and Snoke, 2007). Eocene extension likely initiated development of mylonites within the RMCC shear zone, during which high grade metamorphism persisted (Sullivan and Snoke, 2007). Two syn-extensional plutonic pulses occurred during this time. The first from ~36-40 Ma includes the Harrison Pass Pluton (Dokka et al., 1986; Kistler et al., 1981) (Fig. 4) and the second plutonic pulse occurred at 29 Ma (Wright and Snoke, 1993).

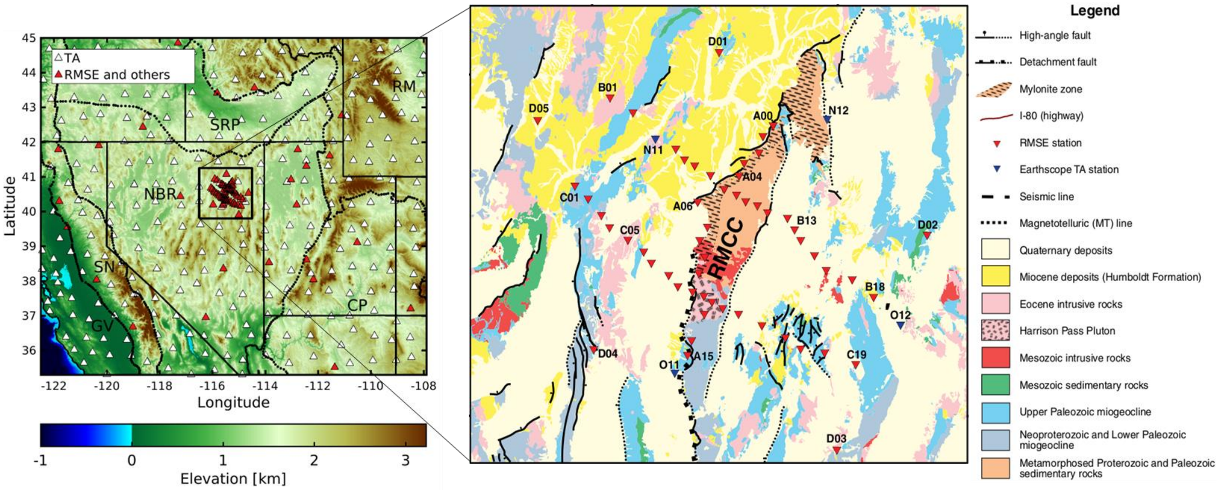

Figure 4. Geologic map of the RMCC region modified after Litherland and Klemperer, (2017).

The mylonitic shear zone that accommodated ductile strain in the past and the more recent brittle slip bounds the Ruby Mountains on its northwest flank adjacent to the RMCC (Fig. 4). A steep eastward dipping normal fault bounds its east side (Fig. 4). Relative to fault slip rates in the Miocene of ~2.6 mm/yr (Haines and van der Pluijm, 2010) recent fault slip rates are much slower, < 0.2mm/yr (Pérouse and Wernicke, 2017; USGS, 2018).

Exposed rocks in the southern Ruby Mountains include low grade to unmetamorphosed Neoproterozoic and Paleozoic sedimentary rocks and plutonic rocks from the Mesozoic and Eocene (Crafford, 2007). Rocks in the Northern Ruby Mountains include metamorphic Proterozoic and Paleozoic rocks (Crafford, 2007). Unlike many other MCC, the RMCC is exceptional in that it exposes rocks below the mylonitic shear zone. Exposures of these rocks are located in the northern portion of the Ruby Mountains. Because the RMCC is polygenetic these metamorphic rocks are Oligocene, Cretaceous, and Jurassic in age with Paleozoic, Proterozoic and Archean protoliths

(Crafford, 2007). The rocks of the northern Ruby Mountains formed at progressively deeper crustal depths, between 13 (Hudec, 1992) and 30 km (McGrew et al., 2000), compared to rocks of the southern Ruby Mountains. This pattern is consistent with an increasing northward widening, up to 1 km, mylonitic shear zone (MacCready et al., 1997) and northward increasing rock formation pressure and temperature (P-T) conditions.

2.4 Surface Waves

Surface waves travel along Earth's surface and arise out of body wave interactions at the free surface. Two types of surface waves, Rayleigh and Love, vary in their polarity and speed. Rayleigh waves exhibit longitudinal and radial polarization whereas Love waves are transversely polarized and usually travel faster than Rayleigh waves at long periods. Surface waves are quite useful for constraining Earth's shallow structure. This is mainly because surface waves are dispersive, meaning the velocity of a surface wave is a function of wave period (Fig. 5).

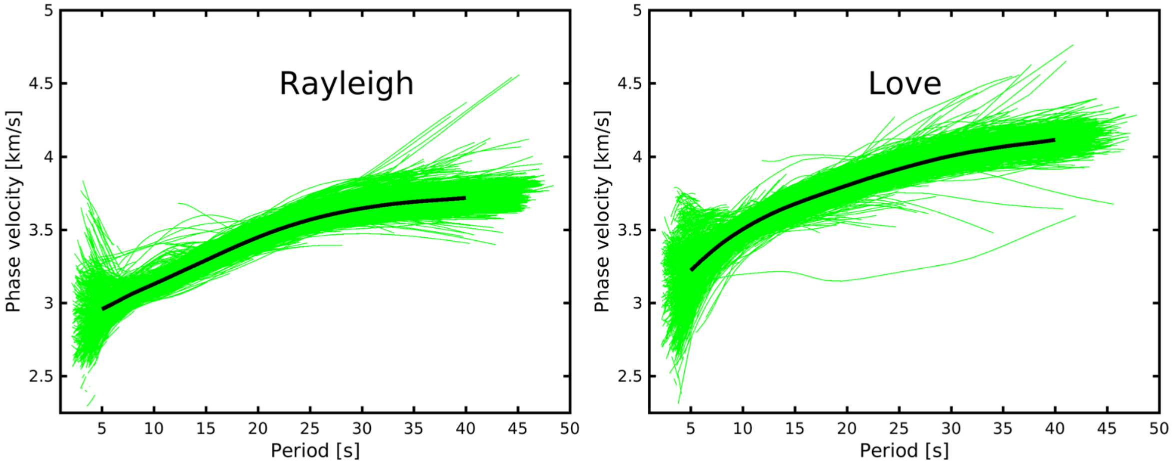

Figure 5. 2,868 vertical (Rayleigh, left) and 2,820 transverse (Love, right) interstation dispersion curve results from frequency-time analysis (FTAN) (green lines) and their means (black lines). Even though there are 3,260 individual ambient noise interstation time series there are less than 3,260 interstation dispersion curves, this is because FTAN has its own methodology for quality control Bensen et al., (2007).

Longer periods are sensitive to greater depths and because rigidity and density increase with depth, longer periods generally travel faster (Shearer, 2009). Sensitivity kernels show the relationship between dispersive velocities and Earth's structure (Fig. 6). Sensitivity kernels depend on local velocity and density structure of the Earth but an approximate empirical relationship shows that period, T, will usually be most sensitive to depths between ~0.75T – 1.5T. Thus, for geologic purposes longer periods can generally be thought to sample deeper structure. Measurement of the propagation of the peak in the surface wave envelope (wave energy) provides group velocity while measurement of the propagation of the individual surface wave peaks or troughs gives phase velocity (often denoted as c).

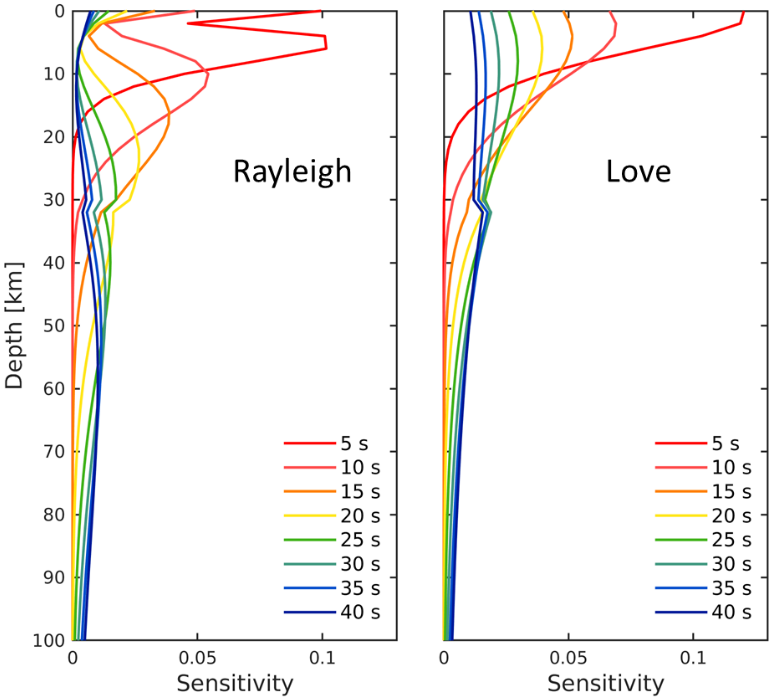

Figure 6. Sensitivity kernels for fundamental mode Rayleigh and Love waves with respect to S-wave velocity dc/dVs. Calculated with senskernel-1.0 using the model US.2016 (Shen and Ritzwoller, 2016) for point 40.6°, -115.4° below the Ruby Mountains. Calculation omits intrinsic shear Q and does not consider sedimentary basins. Peaks of sensitivity correspond to a range of depths. Note that long periods are sensitive to deeper depths.

2.5 Anisotropy

There are two general structural origins for seismic anisotropy, lattice preferred orientation (LPO), and shape preferred orientation (SPO) (Fig. 7) (Shearer, 2009). LPO results from non-random orientation of intrinsically anisotropic minerals. Olivine, which composes much of Earth's mantle, can exhibit > 20 % anisotropy in single crystals (Babuska and Cara, 1991) so even a moderate degree of preferential alignment or fabric organized by strain can produce measurable anisotropy (Long and Becker, 2010). Mica, an assemblage of crustal minerals (e.g Muscovite and Biotite) that are common, >13% (Nesbitt and Young, 1984), in crustal rocks can have ~60 % Vp and ~100% Vs anisotropy (Almqvist and Mainprice, 2017; Babuska and Cara, 1991). SPO is the alignment of

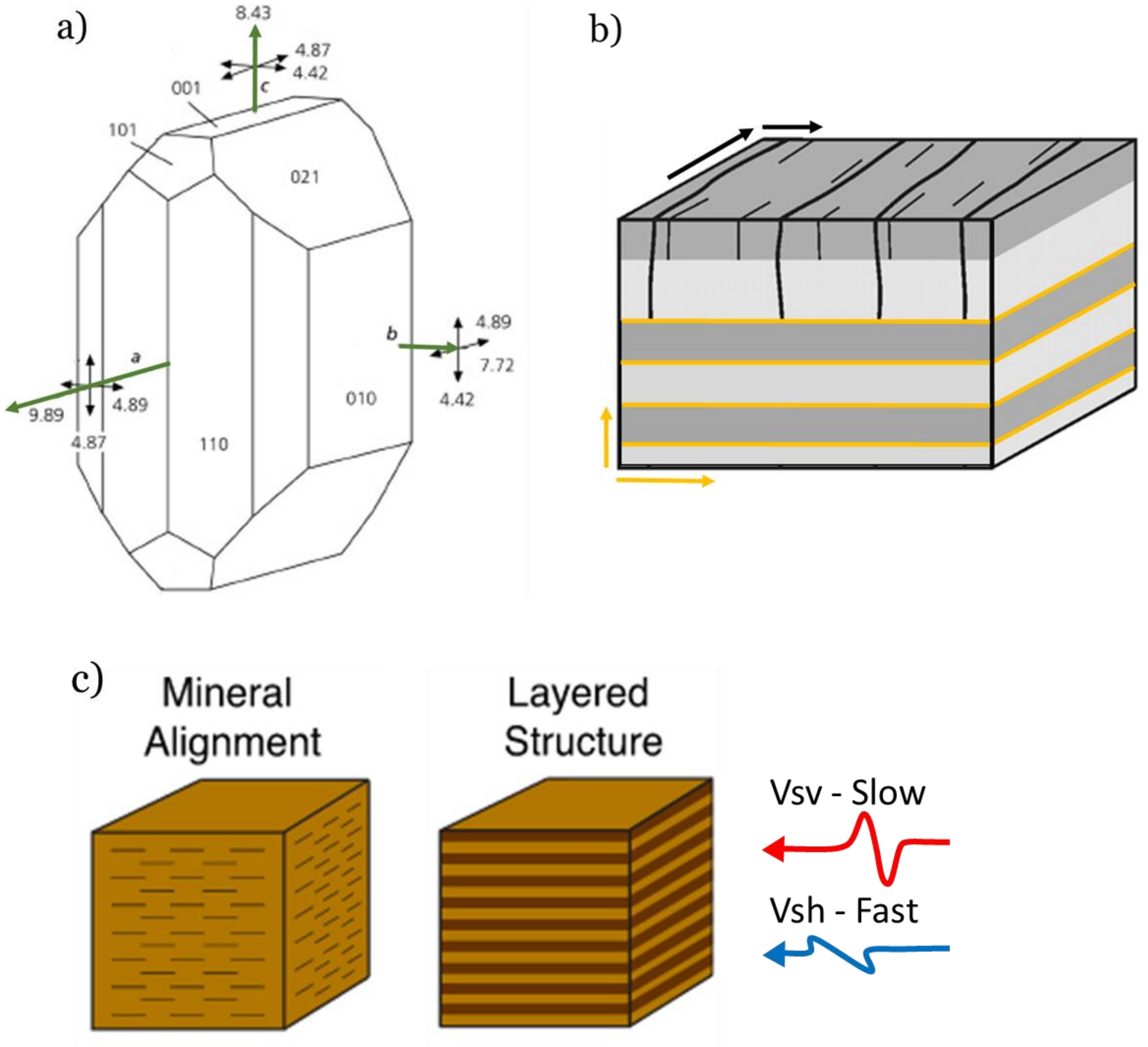

Figure 7. Sources and classification of seismic anisotropy in the Earth. The single olivine crystal in a) is one example of the intrinsic anisotropic properties inherent to many of the minerals that compose the Earth. Green arrows represent the varying velocities (km/s) of a P-wave depending on the direction with which it propagates through the crystal. Black arrows perpendicular to blue arrows show S-wave velocities (km/s) and their respective wave speed variations dependent on polarizations. Modified after Babuska and Cara, (1991). Lattice preferred orientations (LPO) of anisotropic minerals arise from non-random alignment of crystals due to organized strain causing a statistical fast axis within these crystal aggregates/rock fabrics. The shape preferred orientations (SPO) of anisotropy in b) show how seismic anisotropy can arise out the contrast of isotropic materials with distinct elastic properties. Orientations of arrows show anisotropic fast axis and their lengths represent relative magnitude of anisotropy. Black arrows show that waves will usually travel faster parallel to the maximum compressive stress axis. Orange arrows show that bedding planes can also give rise to seismic anisotropy. Stress and bedding plane induced anisotropy are just two examples of SPO of seismic anisotropy. Two commonly invoked interpretations of a positive radial anisotropy signal include c) mineral alignment (LPO) and horizontal layerings (SPO). Modified after Lynner et al., (2018).

materials with distinct elastic properties such that the individual components may be isotropic but the way the components are organized results in anisotropic properties at larger scales. Bedding planes, structures such as faults, melt pockets elongated in one or two dimensions, stress-controlled cracks and joints, and compositional banding, and are all possible ways to generate SPO anisotropy (e.g., Backus, 1962) (Fig. 7 b, c). It should be noted that at deeper crustal depths, due to increasing pressure, cracks and joints from stress are thought to close (Babuska and Cara, 1991). Therefore, stress-controlled fracture orientations are unlikely to cause anisotropy at the middle-to-lower crustal depth range that is the focus of this study. It is also important to note that SPO and LPO are sensitive to both frozen-in and actively evolving fabrics.

Three commonly used techniques to measure seismic anisotropy include the splitting of shear waves, and radial and azimuthal anisotropy from surface waves. Shear wave splitting is perhaps the most popular of seismic anisotropy investigations. Shear wave splitting exploits the fact that shear waves, when propagating through an intrinsically anisotropic material will split into two orthogonal quasi S-waves and one will travel faster than the other. Litherland and Klemperer, (2017) conducted a shear wave splitting study as part of their analysis on the RMCC using the RMSE. With the exception of a few E-W oriented fast axes west of the RMCC they found systematic NE-SW fast axes, which agree with regional shear wave studies and likely reflect deep asthenospheric flow rather than lithospheric deformation. Inability to resolve lithospheric deformation is likely due to the fact that measurements of shear wave splitting have inherently poor depth resolution and the depth integrated signal from the crust may be smaller than that of the upper mantle.

An overarching goal of this study is to constrain anisotropy as a function of depth below the RMCC. Measurements of seismic anisotropy using surface waves provide good depth resolution and are practical for studies at the scale of the continental crust. Surface waves allow for measurement of both azimuthal and radial anisotropy. Azimuthal anisotropy measures wave speed variation with azimuth thus requiring measurements from diverse source-receiver orientations. Radial anisotropy, or transverse isotropy with a vertical symmetry axis, measures wave speed variation arising from polarity differences between Love and Rayleigh waves which are sensitive to V_{SH} and V_{SV} respectively. Positive radial anisotropy occurs when horizontal polarizations are faster than vertical polarizations SH>SV. It follows that negative radial anisotropy is defined as SH<SV. Radial anisotropy is particularly useful for resolving vertical or horizontal layering smaller than a wavelength.

Regional radial anisotropy studies show strong, upwards of 5%, positive radial anisotropy in the middle and lower NBR crust (Moschetti et al., 2010) hypothesized to be sourced from LPO of mica and amphibole. Anisotropy due to LPO is thought to be significant in the middle and lower crust (Christensen and Mooney, 1995). Typical crustal rock assemblages can contain between the range of 1% and 22% anisotropy (Brownlee et al., 2017).

2.6 Ambient noise

In seismology or other types of time series analysis, noise can generally be thought of as any signal other than the signal of interest, which in seismology is usually waves generated by earthquakes or explosions. Ambient seismic noise or the continuous ground motion time series recorded by seismometers between events like earthquakes mainly emanates from ocean waves, cultural noise (e.g. vehicles), wind, and atmospheric effects (Shearer, 2009). The theoretical basis for seismic noise interferometry began to be established early in the development of the field of seismology (Aki, 1957,1965), but there was a long hiatus before further theoretical and empirical analysis led to widespread applications. Vast improvements in computational power and availability of continuous broadband seismic data set the stage for more recent advances including theoretical proofs that showed the empirical Green's function emerges in correlations of a diffuse wave field created by many weak stochastically distributed sources (Lobkis and Weaver, 2001). This was followed by pioneering applications that showed, over time (months to years), these empirical Green's functions estimated from ambient noise yield clear dispersive surface waves, consistent with surface waves excited by earthquakes (Shapiro et al. 2005). Use of ambient noise to recover Rayleigh and Love wave data provides exceptional benefits compared to more traditional earthquake-based techniques. These benefits include, the ability to obtain surface wave data in the absence of earthquakes, increases in tomographic resolution due to increased number of source-receiver paths and control over virtual source locations, and access to shorter periods providing constraints on crustal shear velocity that were rarely accessible in the past. For all these reasons ambient noise surface wave imaging has become a large and still growing research direction in modern seismology. Here, we use ambient noise interferometry to obtain Rayleigh and Love wave dispersion curves.

3 DATA

This study analyzed continuous time series data from a recent EarthScope Flexible Array passive seismic deployment, known as the Ruby Mountains Seismic Experiment (RMSE; Litherland and Klemperer, 2017) and surrounding networks. The RMSE deployed 50 three-component broadband seismometers spaced approximately 5-10 km apart along 3 transects between 2010 – 2012 (Fig. 1). Permanent stations used from surrounding networks (AZ, CA, CO, ID, NV, OR, UU; Fig. 1) are three component broadband seismometers that operated contemporaneously with the RMSE. The surrounding network stations are azimuthally dispersed with respect to the dense RMSE and separated from the RMSE by ~100 – 700 km (Fig. 1). We combined our analysis with measurements from a previous study (Ekström, 2014; USANT) that similarly analyzed data from the USArray Transportable Array (TA). TA stations were deployed within our region of study from 2005 to 2008 providing additional three-component broadband seismometer coverage with a nearly uniform spacing of ~70 km. Data for this study were accessed through the Incorporated Research Institutions for Seismology (IRIS) Data Management Center.

4 METHODS

4.1 Noise correlations

The increase in the use of ambient noise for large scale detailed tomography prompted a generalized signal processing technique (Bensen et al., 2007). This study generally follows this method to process approximately 18 months of ambient noise data recorded on the vertical (Z) and horizontal (N, E) components of the RMSE and surrounding network permanent stations, ~75 stations, resulting in 3260 noise correlations. Minor modifications to the processing were made by whitening the signal spectrum without applying any time-domain amplitude normalization (e.g., Ekström, 2014) and using shorter time windows in order to obtain a larger sample size for averaging normalized cross-correlations from each time window (Seats et al., 2012). All time series data were down sampled to 5 samples per second before cross correlation. Component rotation is required to obtain accurate Rayleigh (R-R) and Love (T-T) wave data from the cross-correlations. Following Lin et al., (2008) rotation is completed after cross-correlation using the following equation (1):

$$\begin{bmatrix}TT\\RR\\TR\\RT\end{bmatrix} = \begin{bmatrix} -\cos\theta\cos\Psi & \cos\theta\sin\Psi & -\sin\theta\sin\Psi & \sin\theta\cos\Psi \\ -\sin\theta\sin\Psi & -\sin\theta\cos\Psi & -\cos\theta\cos\Psi & -\cos\theta\sin\Psi \\ -\cos\theta\sin\Psi & -\cos\theta\cos\Psi & \sin\theta\cos\Psi & \sin\theta\sin\Psi \\ -\sin\theta\cos\Psi & \sin\theta\sin\Psi & \cos\theta\sin\Psi & -\cos\theta\cos\Psi \end{bmatrix} \mathrm{X} \begin{bmatrix}EE\\EN\\NN\\NE\end{bmatrix}$$

The resulting stacked cross-correlations confirm the isolation of Love and Rayleigh waves and nicely show the dispersive nature of surface waves (Fig. 8).

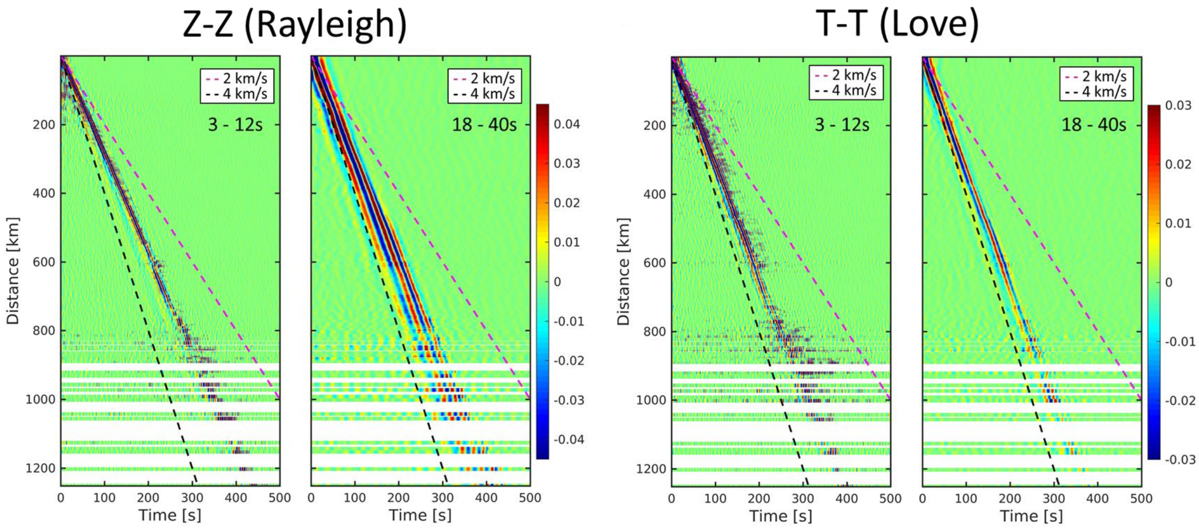

Figure 8. Stacked distance versus time images of 3260 noise cross correlations recorded over ~18 months for the RMSE and exterior stations (Red triangles in topography figure). The stacks show the Z-Z and T-T correlated components band pass filtered at 3-12 s and at 18-40 s. The figure nicely shows the dispersive nature of surface waves and the isolation of Love waves, seen in faster velocities than that of Rayleigh waves.

4.2 Dispersion curves

Surface wave velocities as a function of period (dispersion curves) are recovered using frequency-time analysis (FTAN) (e.g., Dziewonski et al., 1969). This a common method that has proven robust in its efficiency and accuracy. Following Bensen et al., (2007) we use an automated FTAN technique. Outputs from this step include interstation phase and group velocities over a period range between 3 and 40 s. For the purposes of this study we use phase velocities for tomography (Fig. 5). The signal-to-noise ratio (SNR) is defined as the ratio between the maximum amplitude within the signal window and the root-mean-square (RMS) amplitudes within the noise window. We apply three types of quality control parameters to the dispersion curves to ensure that: (1) phase velocity, c, is between 2 – 5 km/s; (2) SNR is > 6; and (3) the interstation distance is >2 wavelengths.

4.3 Phase velocity tomography

To maximize path coverage and quality of phase velocity maps we combined our new quality-controlled dispersion curves with dispersion curves from a previous regional study that used TA data (USANT; Ekström, 2014). We used the USANT phase velocity maps to predict all inter-station phase velocity measurements and only retained measurements whose travel time percentage misfits were < 2 standard deviations from the mean of the combined measurements (Fig. 9). Smoothing and norm damping were included in the least-squares inversion of the final culled inter-station travel times and the weight of the regularization parameters was chosen using trade-off curve analysis. Based on the RMCC focus of this study and the geometry and density of interstation paths (Fig. 9) we prioritize results within a ~90,000 km^2, area centered on the RMCC. The resulting phase velocity maps agree well with the USANT model but provide finer resolution in our study region (Fig. 10). Rayleigh and Love wave phase velocity maps are calculated at 5, 6, 8, 10, 12, 15, 20, 25, 30, 35, and 40 s periods using a latitude grid spacing of 0.15° and a longitude grid spacing of 0.2° (Fig. 11). Estimated phase velocity uncertainty (Table 1) was adopted from Jiang et al., (2018).

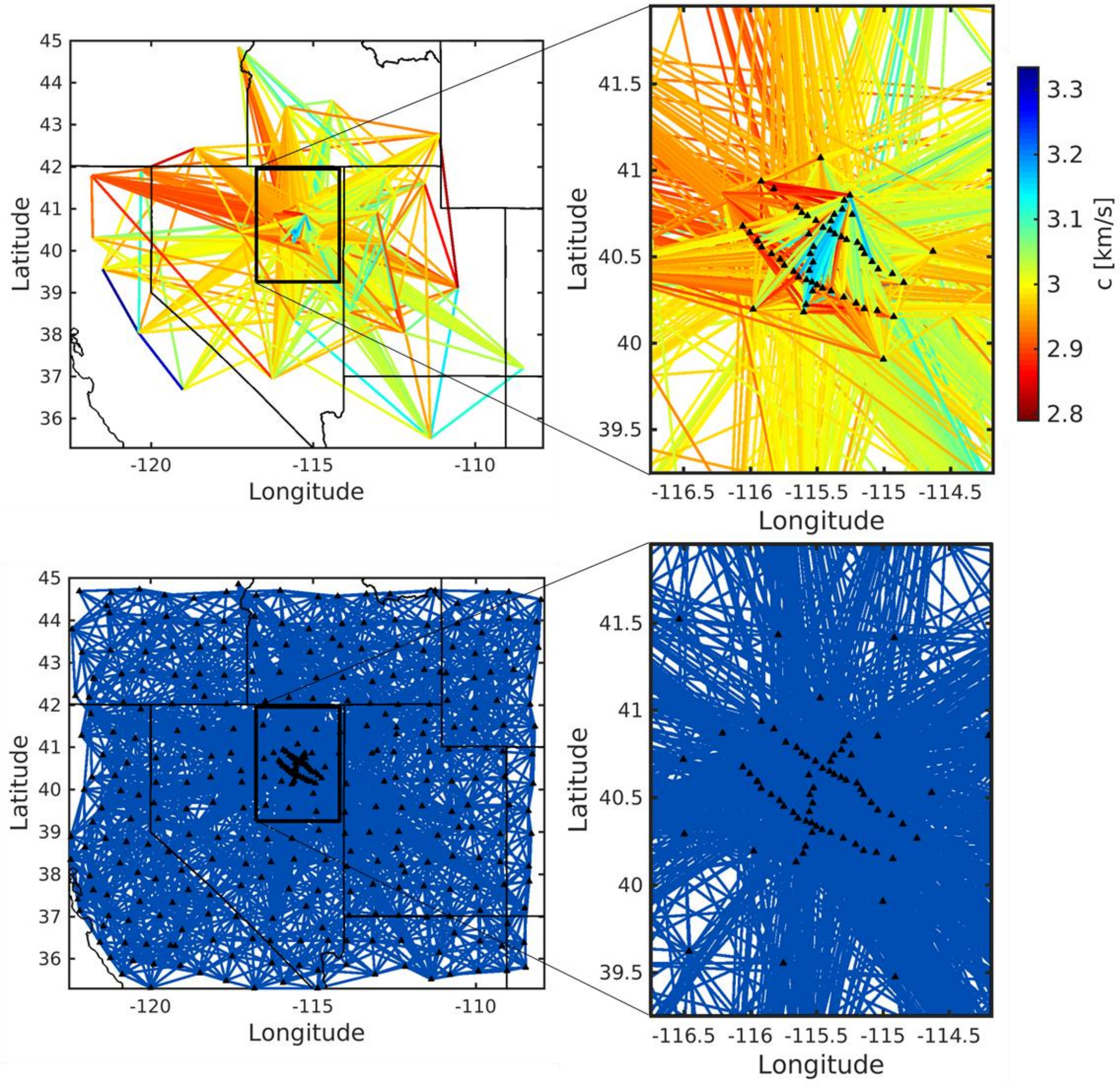

Figure 9. Interstation phase velocity values and path coverage used for phase velocity tomography at a 6 s period. Top row shows retained interstation phase velocity values and paths calculated in this study. Notice high density of interstation paths in the study region and high velocities that coincide with the location and strike of the RMCC. Bottom row shows interstation phase velocity paths after combination with USANT measurements. Notice increased regional path coverage and increased number of crossing paths within study region.

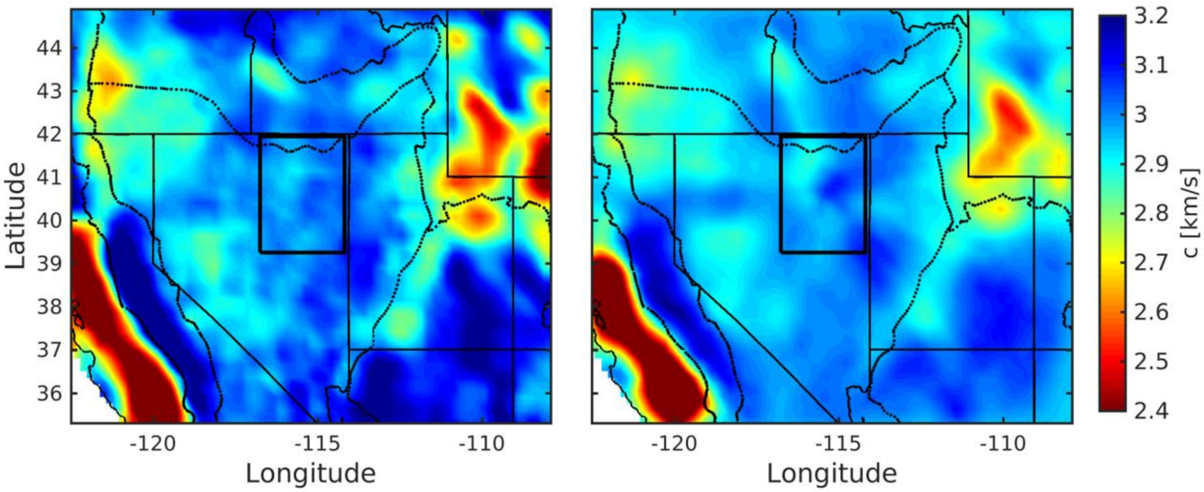

Figure 10. Comparison of 6 s phase velocity, c, tomographic maps from USANT (left) and this study (right). The maps agree well and resolve crustal structure associated to physiographic provinces particularly the Great Valley, Sierra Nevada, and Colorado Plateau.

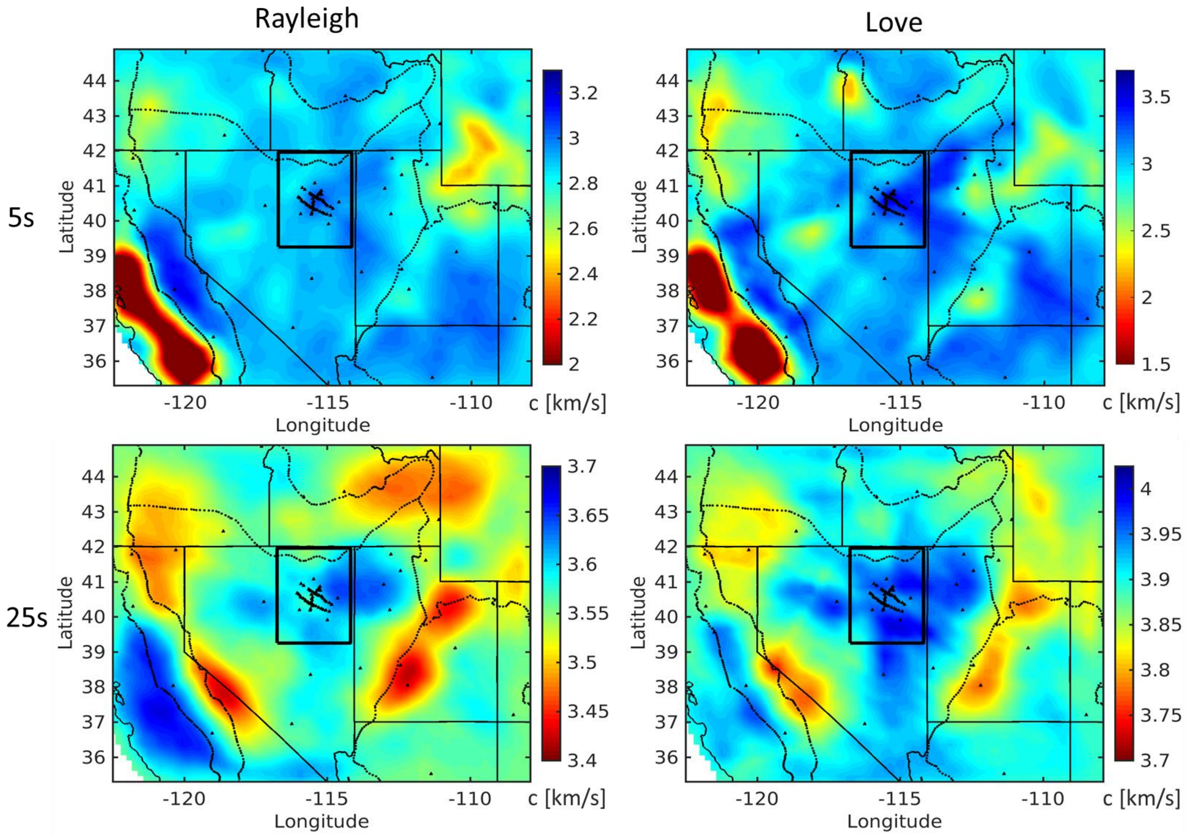

Figure 11. Regional Love and Rayleigh wave phase velocity maps at 5 and 25 s period.

Period	Rayleigh error	Love error
5	.050	.039
6	.045	.040
8	.044	.035
10	.043	.033
12	.038	.032
15	.037	.032
20	.038	.033
25	.039	.032
30	.036	.029
35	.036	.029
40	.036	.029

Table 1. Table of phase velocity errors for given period adopted from Jiang et al., (2018).

4.4 Probabilistic Vs and anisotropy inversion

Using piercing points through the phase velocity maps (Fig. 12) a set of observational dispersion curves is generated, which provides the input data for 1D Vs inversions beneath each point in the geographic model domain. These observed dispersion curves and their respective errors (Table 1) are inverted with a Bayesian Markov chain Monte Carlo (BMMC) method (Herrmann, 2013; Shen et al., 2012). This inversion technique estimates Vs structure and radial anisotropy as a function of depth and geographic location by allowing independent variations in V_{SV} and V_{SH} (Fig. 13).

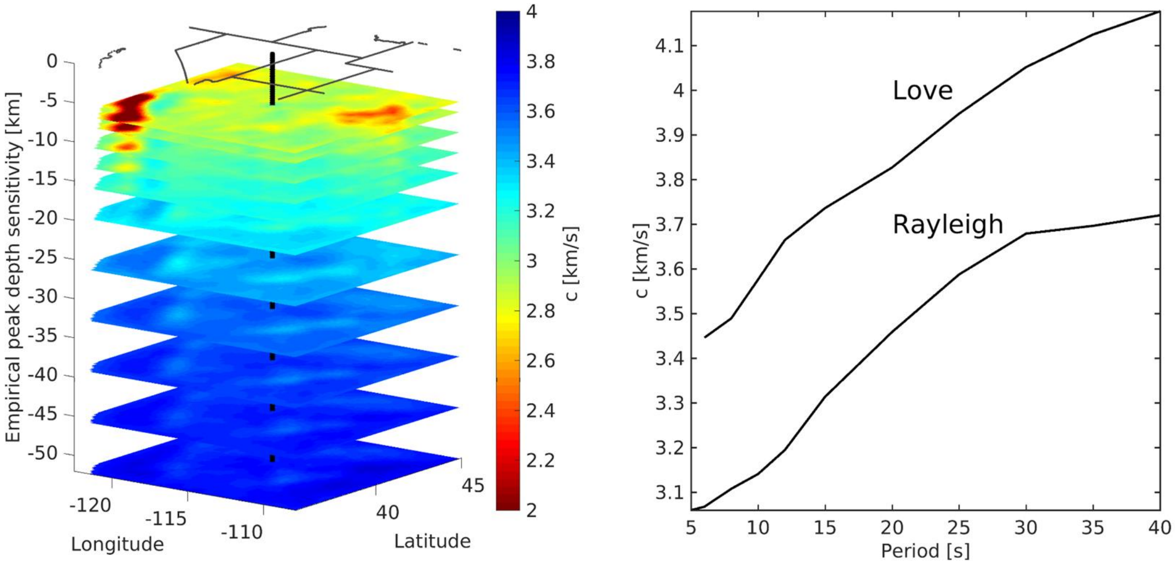

Figure 12. Visual example of inversion input as a function of depth and geographic location. Left) Calculated (5-40s) Rayleigh wave phase velocity maps being pierced (black line) at point 40.6 -115.4 centered on the RMCC and right) the corresponding dispersion curves.

One of the benefits of BMMC inversion technique is the lack of dependence upon a starting model. The inversion samples a uniform prior distribution of parameter values within ranges defined in Table 2 to find a set of acceptable models, or posterior distribution, using chi-squared misfits and the Metropolis - Hastings algorithm (Hastings, 1970; Mosegaard and Tarantola, 1995). First the inversion was run under the assumption of isotropy ($V_{SV} = V_{SH}$) (Supplementary Fig. 1). To reduce the chi-squared misfit and quantify radial anisotropy a second BMMC inversion was performed using 10 model parameters, four b-splines in the crust and one half space in the mantle for both V_{SV} and V_{SH} (Table 2). We implement a prior constraint that requires radial anisotropy be no less than -20 % and no greater than 20 %. This constraint has a physical basis and reduces computational time. In both isotropic and anisotropic inversions, velocity is allowed to freely increase or decrease with depth.

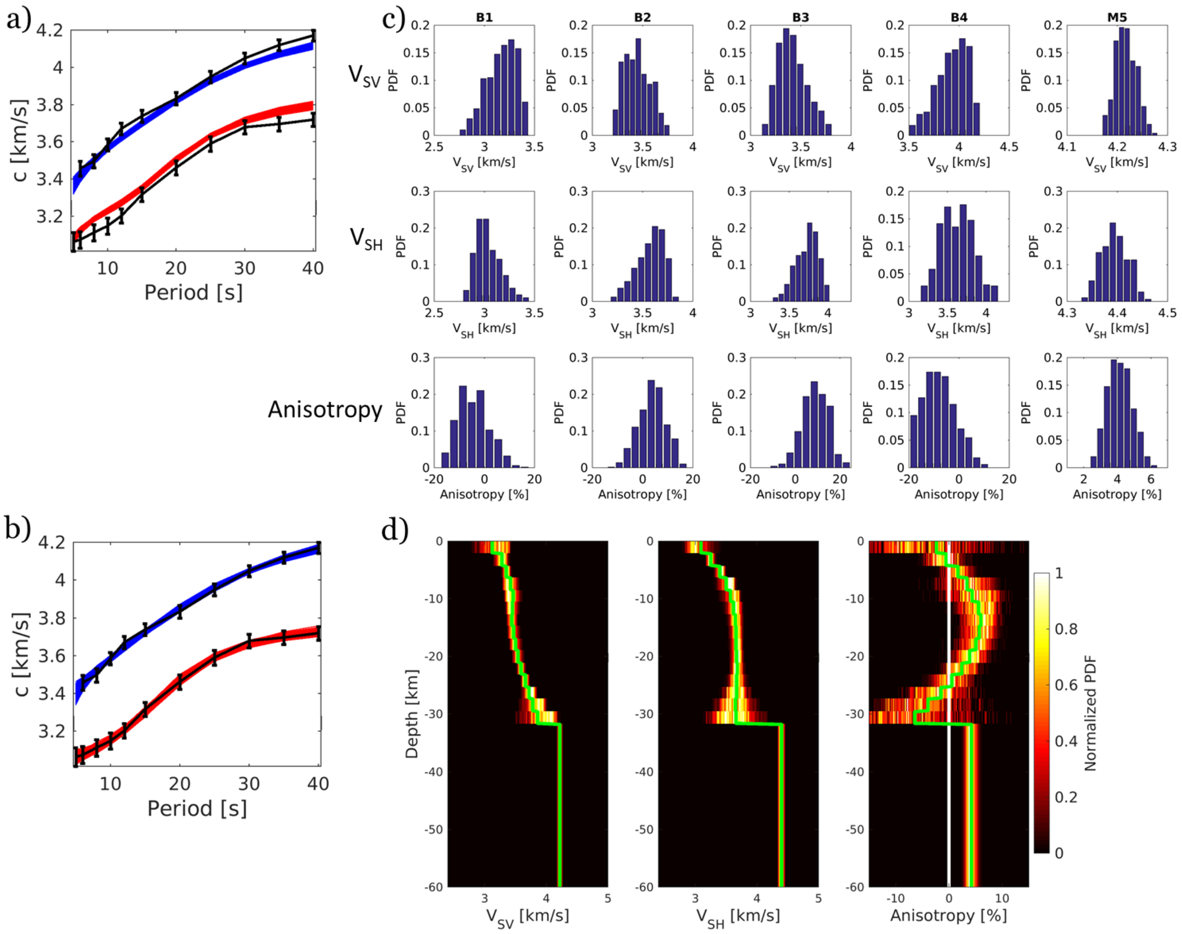

Figure 13. 1D BMMC inversion results from piercing point 39.6°, -115.4° (same as Fig. 12) centered on the RMCC. a) Observed (black lines) and predicted Love (blue lines) and Rayleigh (red lines) wave dispersion curve from an isotropic BMMC inversion. Observation error bars are from table 1. Notice predicted curves do not fit observed curves well. b) Same as a) but with an anisotropic parameterization in the BMMC inversion. Notice anisotropic predictions fit observations well. c) Probability density functions (PDFs) of the 10 model parameters, four b-splines in the crust (B) and one half space in the mantle (M) for both V_{SV} and V_{SH}, used in the anisotropic BMCC inversion (see table 2). Bottom row is anisotropy which is not a parameter within the inversion but is calculated using equation 2. d) Posterior probability distribution as a function of depth for V_{SV}, $V_{SH,}$ and anisotropy. Green line is the mean of the posterior distribution.

Model variable	**Lower bound**	**Upper bound**
1st B-spline coefficients of crust	2.5 km/s	3.5 km/s
2nd B-spline coefficients of crust	2.8 km/s	3.8 km/s
3rd B-spline coefficients of crust	2.8 km/s	4.0 km/s
4th B-spline coefficients of crust	3.0 km/s	4.2 km/s
Half space of the mantle	3.9 km/s	4.8 km/s
Constraints		
Moho depth	Model dependent	Model dependent
Anisotropy	-20 %	20 %

Table 2. Prior model space and constraints.

Each 1D inversion produces a set of predicted dispersion curves (Fig. 13 a, b) and the posterior probability distribution of inverted parameters, V_S for isotropic, V_{SV} and V_{SH} for anisotropic (Fig. 13 c, d). Radial anisotropy, RA, is calculated from the Rayleigh-Love discrepancy using a Voigt average in equation (2):

$$RA = \frac{100(V_{SH} - V_{SV})}{\sqrt{\frac{2}{3}(V_{SV})^2 + \frac{1}{3}(V_{SH})^2}}$$

The mean of the posterior distribution is taken to be the final model (Fig. 13 d). 1D inversions are done iteratively at 266 piercing points each spaced 0.15° x 0.2° apart, thus averaging over ~350 km^2, to form a 3D Vs and anisotropic model below the RMCC. We do not include anisotropy as a parameter within the inversion. Instead, we explore the effects of crustal thickness by running both the isotropic and anisotropic inversions using three regional crustal thickness models (Schmandt et al., 2015; Schutt et al., 2018; Shen and Ritzwoller, 2016), denoted as A, B, and C respectively in following figures, and an interpreted local crustal thickness model calculated below each station within the RMSE (Litherland and Klemperer, 2017). This approach reduces the likelihood of overfitting the data by limiting the number of model parameters included within the inversion. We do not explicitly parameterize sedimentary basins within the inversions because shorter period dispersion measurements would be needed for accurate constraints and basin structure is not a focus of this study. Love wave phase velocities at 5 s were not incorporated into the inversion because some areas showed suspicious increases in phase velocity with decreasing period from 6 to 5 s.

5 RESULTS

5.1 Phase velocity maps

At a 5 s period, upper crustal depths, regional phase velocity anomalies agree with well-known geologic provinces such as the Colorado Plateau, San Joaquin valley, and the Sierra Nevada mountain range (Fig. 11). At a 25 s period, lower crustal depths, the Basin and Range exhibits a fast phase velocity anomaly likely due to the shallow Moho allowing for sensitivity in the mantle. At short periods 5-8 s the shallow core structure of the RMCC makes a clear impact on interstation phase velocity (Fig. 9) contributing to a high velocity region in phase velocity maps at these periods (Fig. 11). Overall, we observe high velocity anomalies at short periods and low velocity anomalies at long periods below the RMCC in both Love and Rayleigh wave phase velocity maps. (Fig. 11)

5.2 Misfit maps

Misfit maps were constructed at each piercing point by taking the mean of the chi-squared misfit of the predicted Love and Rayleigh dispersion curves for the mean of the posterior distribution. Running the BMMC inversion under an isotropic assumption for the three crustal thickness models results in a misfit map mean of 14-16 (Fig. 14). The area directly below the southern portion of the RMCC and a small area southeast of the RMCC report large chi-squared misfit values, > 25 (Fig. 14). Isotropic results from RMSE interpreted local crustal thicknesses have a mean chi-squared misfit of 20.7 and also show large misfit values, > 25, below the southern portion of the RMCC

(Supplementary Fig. 2). The introduction of anisotropy to the BMMC inversion significantly reduced the misfit map mean for the three crustal thickness to between 1.74-2 (Fig. 14). The highest misfit values for these maps 4.1-4.7 locate in the northern portion of the study area. Anisotropic inversion results using RMSE interpreted local crustal thicknesses are also significantly reduced, with a mean misfit of 1.8.

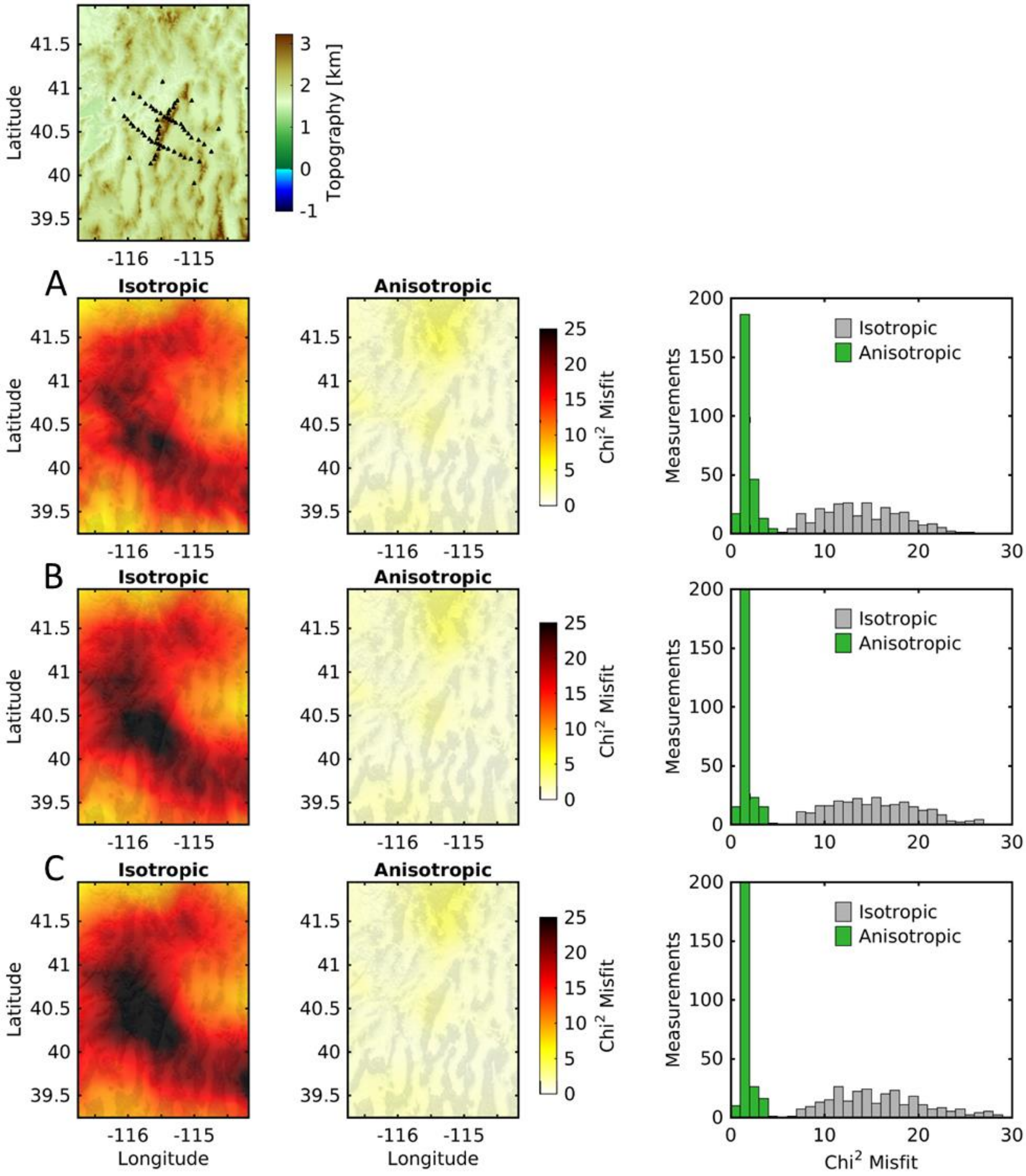

Figure 14. Isotropic (left column) and anisotropic (center column) chi^2 misfit maps for three different crustal thickness models A) Schutt et al., (2018) B) Schmandt et al., (2015) and C) Shen and Ritzwoller, (2016). Right column shows histograms of isotropic and anisotropic chi^2 misfit values. Notice significant chi^2 misfit reduction after anisotropic inversion.

5.3 Vs and radial anisotropy maps

Due to the broad range of depth sensitivity of surface waves (Fig. 6) we average depths of 0-5 km, 5-15 km, and 15 km - Moho, roughly representing the upper, middle, and lower crust respectively. A high Vs anomaly can be observed in the center of the study region at upper crustal depths. This high Vs region is strongly correlated to the location of the RMCC and is likely the metamorphic core of the RMCC. This same area transitions to low Vs in the middle and lower crust and is part of a ~50-100 km wide band that curves out of the SW northward before curving back down to the SE (Fig. 15). Vs structure changes little between the three crustal thickness models.

Accounting for both the reliability and magnitude we plot only anisotropy that satisfies equation (3):

$$\left(|RA| - 2(\sigma)\right) > 0$$

giving the plotted results 95% confidence. Areas where radial anisotropy does not meet this criterion are set to 0 (Supplementary Fig. 3, 4). Positive radial anisotropy ($V_{SH} > V_{SV}$) dominates the depth averaged upper, middle and lower crust maps. Positive anisotropy is grouped in the northern and southern portions of the study area at mainly middle and lower crustal depths (Fig. 16). The northern grouping of anisotropy is diffuse and located in a region where the magnitude of Cenozoic extension is significantly less than the rest of the region (Stewart and Faulds, 1998), extensive Cenozoic volcanic deposits begin (Faulds and Varga, 1998) and BR style Quaternary faulting diminishes (Fig. 17). The anisotropy signal observed in the north diminishes at latitude 42° where the Snake River Plane physiographic province roughly begins. The southern grouping of anisotropy at mid-crustal depths seems to be focused and somewhat correlated to the RMCC. The strongest anisotropic signal, ~6%, is observed in the middle crust (Fig. 16). Negative anisotropy ($V_{SV} > V_{SH}$) is nearly non-existent. As with Vs, patterns of anisotropy do not significantly change when varying crustal thickness in the BMMC inversion. Furthermore, patterns of anisotropy do not seem to correlate with crustal thickness (Fig. 16). Anisotropy in the middle and lower crust occurs in regions where modern strain rates are lowest (Fig. 17) (Kreemer et al., 2012).

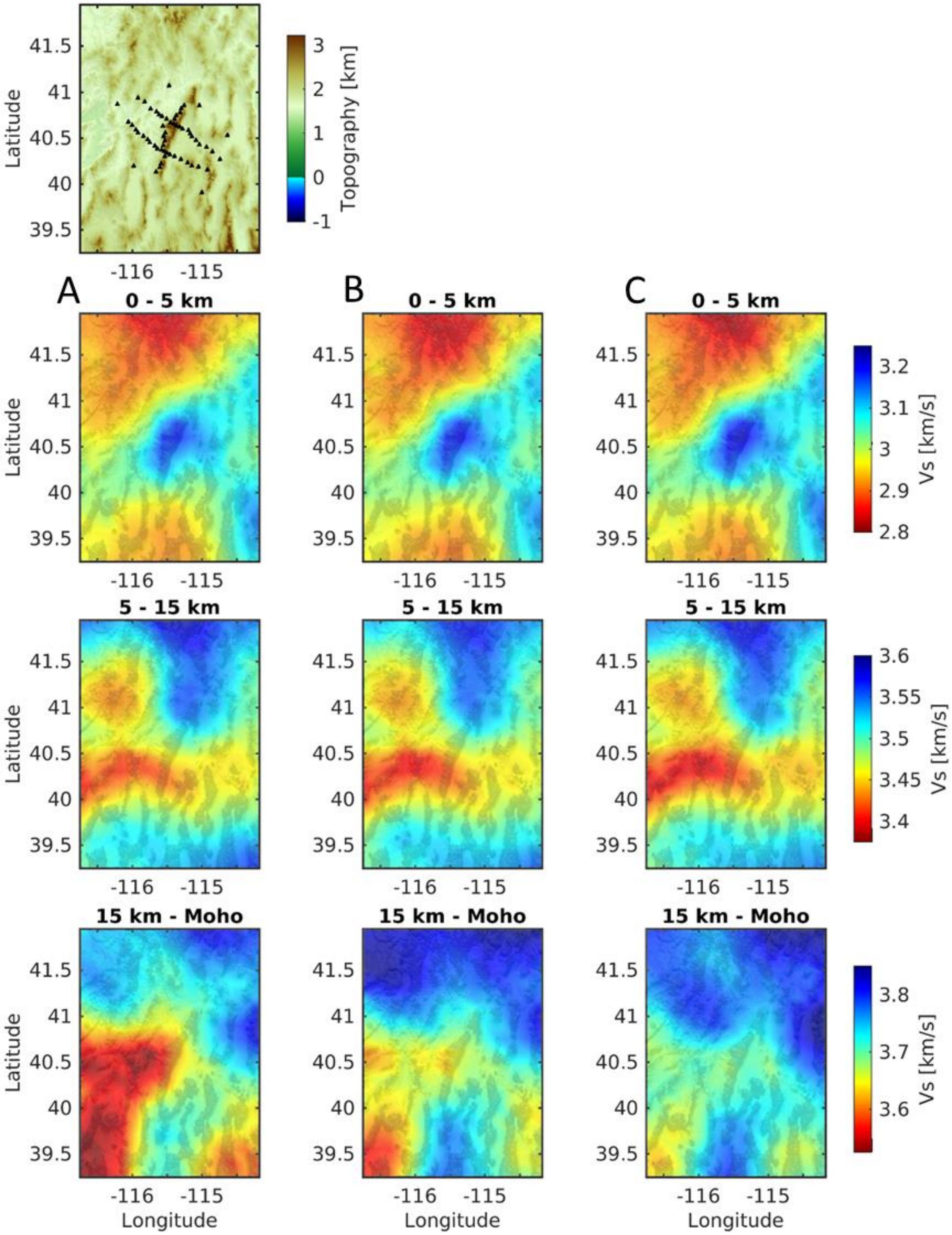

Figure 15. Upper (0-5 km), middle (5-15 km), and lower (15 km -moho) crustal depth averaged Isotropic Vs maps from anisotropic BMMC inversions using crustal thickness models from A) Schutt et al., (2018) B) Schmandt et al., (2015) and C) Shen and Ritzwoller, (2016). Topographic map and RMSE stations (black triangles) serve as a spatial reference. Notice that Vs patterns are consistent throughout the crustal thickness models.

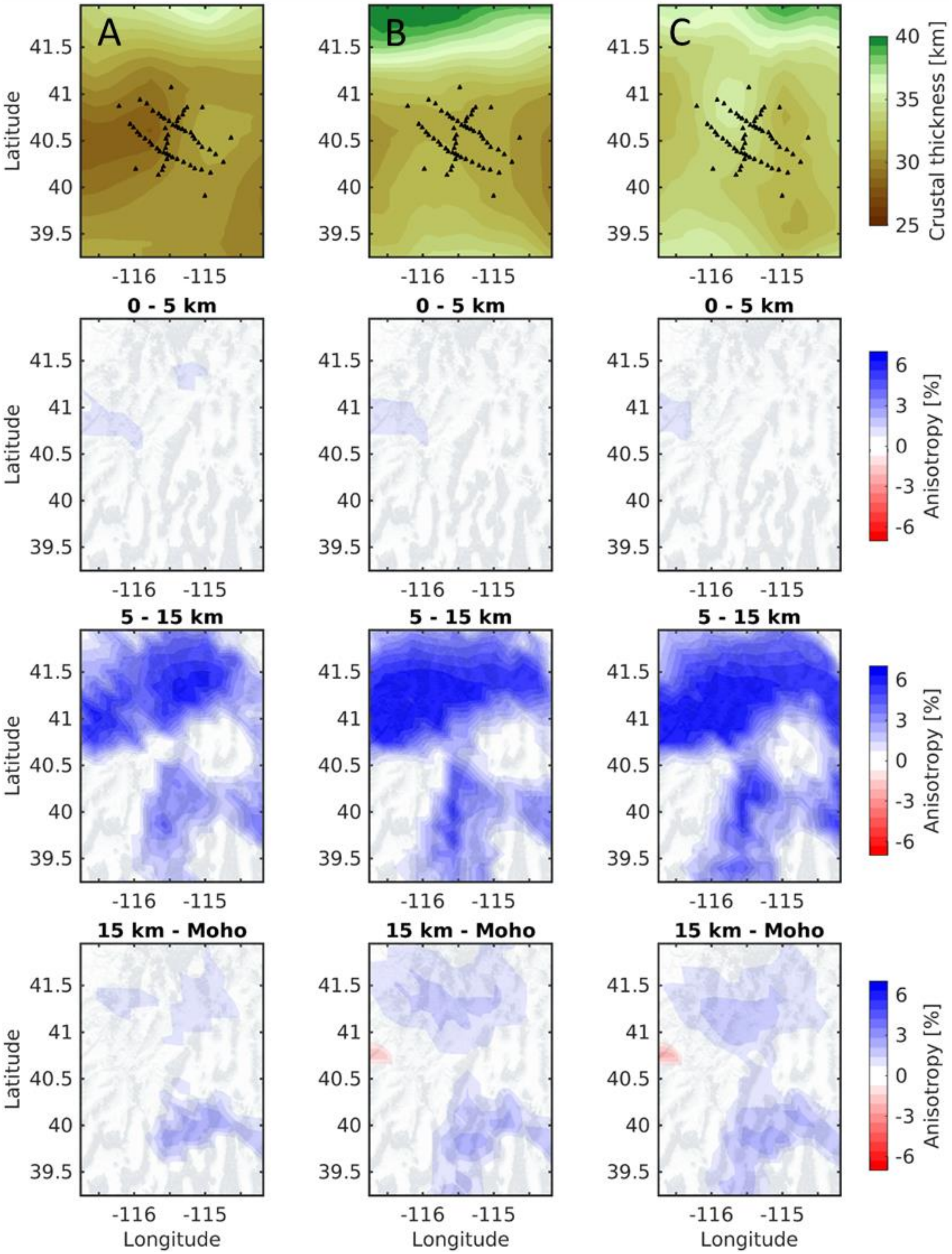

Figure 16. Upper (0-5 km), middle (5-15 km), and lower (15 km - Moho) crustal depth averaged anisotropy maps from BMMC inversions using crustal thickness models from A) Schutt et al., (2018) B) Schmandt et al., (2015) and C) Shen and Ritzwoller, (2016). Only anisotropy that satisfies equation 3 is plotted. Upper row are maps of each of the crustal thickness models and RMSE stations (black triangles) serve as a spatial reference. Notice crustal thickness and anisotropy patterns are not strongly correlated and that patterns of anisotropy are consistent throughout the crustal thickness models.

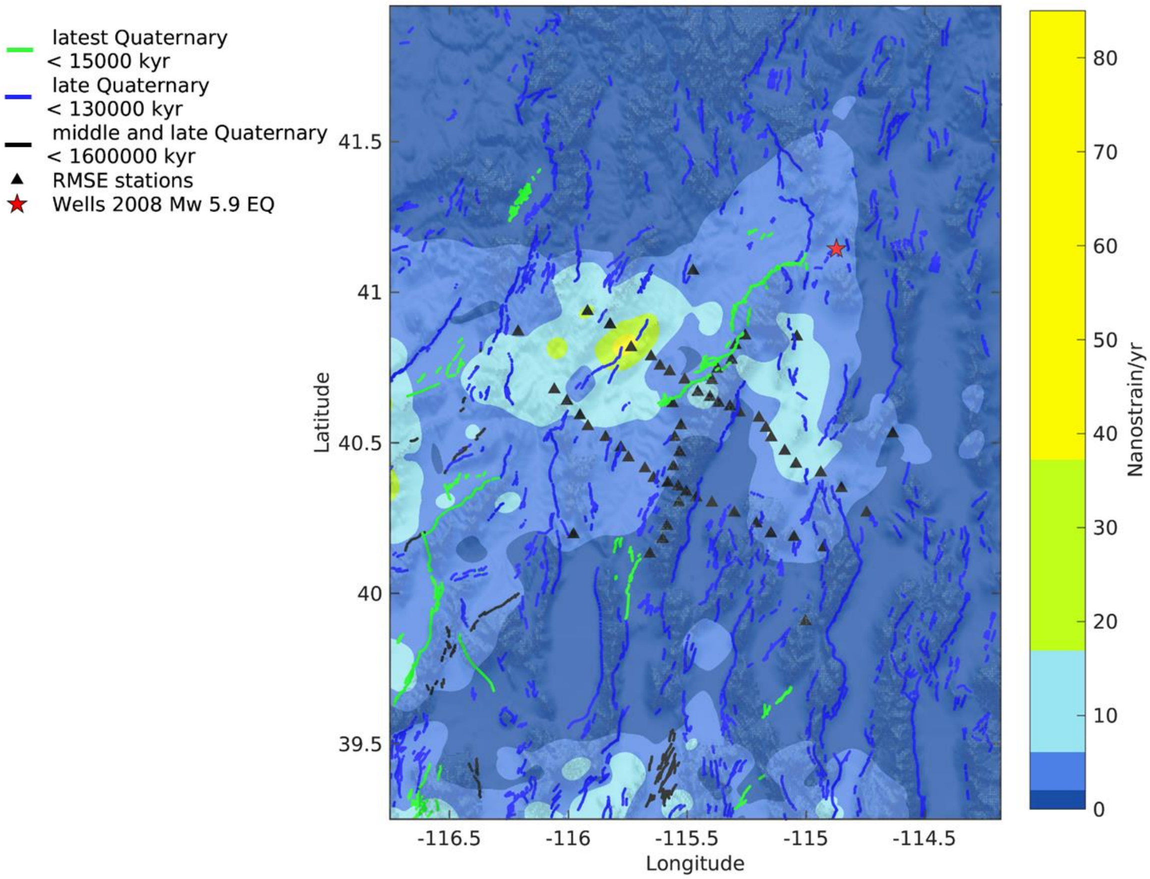

Figure 17. 2nd invariant strain rate in nanostrain/yr of the study region from Kreemer et al., (2012). Lines are Quaternary faults color coordinated by age. Black triangles are RMSE stations. Red star is location of the 2008 Wells, NV Mw 5.9 earthquake.

5.4 Vs and radial anisotropy cross sections

To better characterize patterns of anisotropy with depth and evaluate differences arising from crustal thickness variations we analyze cross sections varying in location and geometry. We construct one cross section striking N-S and one cross section striking E-W (Fig. 1, 18) using the crustal thickness model of (Schmandt et al., 2015). We also construct 3 cross sections approximately parallel to the strike of the 3 RMSE transects (Fig. 1, 19).

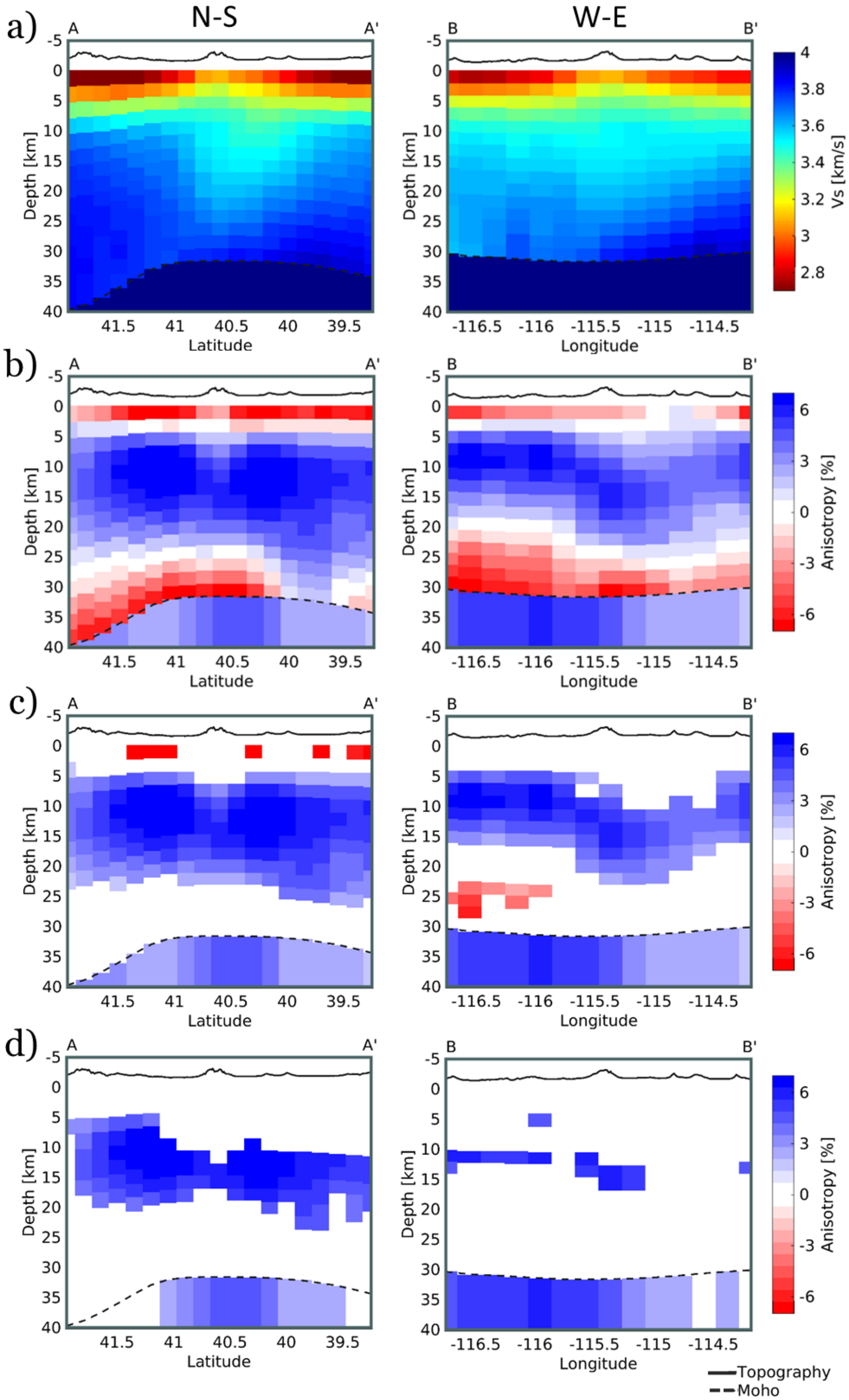

Figure 18. N-S (A-A', left column) and W-E (B-B', right column), cross sections through study area showing Vs and anisotropy results from crustal thickness model A. a) Isotropic Vs and b-d) anisotropy with increasing quality control. b) No quality control, c) Satisfies (|RA|- (σ))>0, and d) Satisfies (|RA|-2(σ))>0, equation 3.

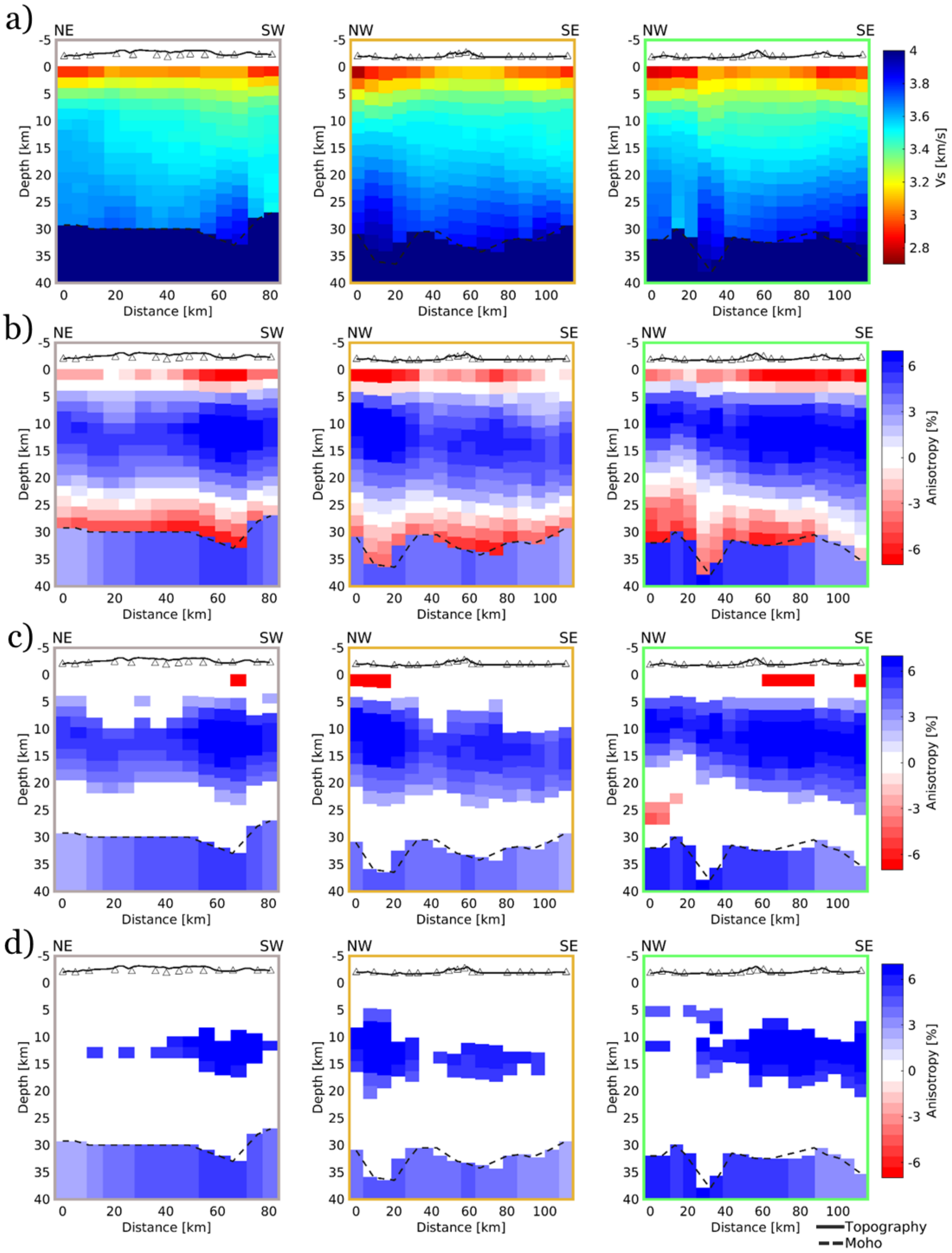

Figure 19. Cross sections through study area using crustal thickness transects from Litherland and Klemperer, (2018). Frame colors correspond to cross section colors in figure 1. a) Isotropic Vs and b-d) anisotropy maps with increasing quality control. b) No quality control, c) Satisfies (|RA|-(σ))>0, and d) Satisfies (|RA|-2(σ))>0, equation 3.

Although the cross-sectional strike and crustal thicknesses used in the inversion vary between figure 18 and figure 19, dominant anisotropy patterns are consistent with anisotropy in map view (Fig. 16). N-S cross sections show that the area directly below the RMCC has a slight pattern of diminished anisotropy relative to the surrounding NBR (Fig. 18). However, an isolated area of ~6% positive anisotropy appears directly below the RMCC in the E-W cross section (Fig. 18). These patterns of anisotropy are inconsistent with each other but can be reconciled by considering map view anisotropy results. Anisotropy maps at deep crustal depths show that the pattern of anisotropy cannot be confidently correlated to the RMCC. Cross section results reveal that positive anisotropy is required in the uppermost mantle and, in agreement with Lin et al., (2011), is uncoupled to crustal anisotropy (Supplementary Fig. 5).

To further illuminate whether anisotropy below the RMCC deviates from regional trends we compare piercing point subset averages, representing the RMCC and surrounding NBR, of anisotropy as a function of depth (Fig. 20). On the whole, and in agreement with anisotropy maps and cross sections, the anisotropy versus depth plots further reveal a persistent trend of ~6 % positive anisotropy throughout middle crustal depths (~5-20 km) below our study area at 95% confidence. Anisotropy in the upper and lower crust is minimal.

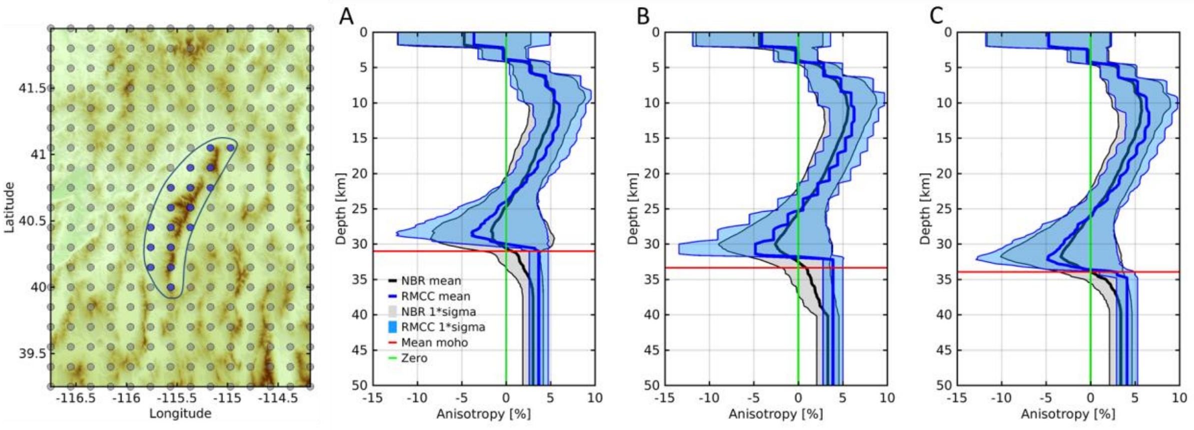

Figure 20. Piercing point subsets, NBR (gray circles) and RMSE (blue circles), used to calculate mean anisotropy depth profiles for A) Schutt et al., (2018) B) Schmandt et al., (2015) and C) Shen and Ritzwoller, (2016). Area between green zero line and shaded regions shows where anisotropy is required using (|RA|- (σ))>0.

6 DISCUSSION

6.1 Anisotropy in crustal minerals

Micas and amphibole are two highly anisotropic (Almqvist and Mainprice, 2017) (Fig. 21) and abundant crustal minerals thought to be influential in observed crustal seismic anisotropy (Mahan, 2006). Micas are the most anisotropic phases in the middle and lower crust (Almqvist and Mainprice, 2017) and recent laboratory experiment on rock samples from MCC, including the RMCC, reveal that bulk rock compositions with the most mica have the highest anisotropy (Erdman et al. 2013). This trend is not observed with amphibole rich rocks from MCC. Furthermore, mica rich rocks trend toward hexagonal symmetry whereas amphibole rich rocks trend toward orthorhombic symmetry (Brownlee et al., 2017). 77% of the 95 crustal rocks from Brownlee et al., (2017) shows slow-axis symmetry. Mica-rich rocks always display slow-axis symmetry but amphibole rich rocks can have fast or slow axis symmetry. In this paradigm LPO alignments from E-W Basin and Range extension would most likely produce a positive radial anisotropy signal as was interpreted by Moschetti et al., (2010). Although dominance of mica is preferred based on the reasons above, both mica and amphibole have the potential of being key contributors to radial anisotropy signals sourced from LPO and are capable of producing the anisotropic patterns we observe in our images.

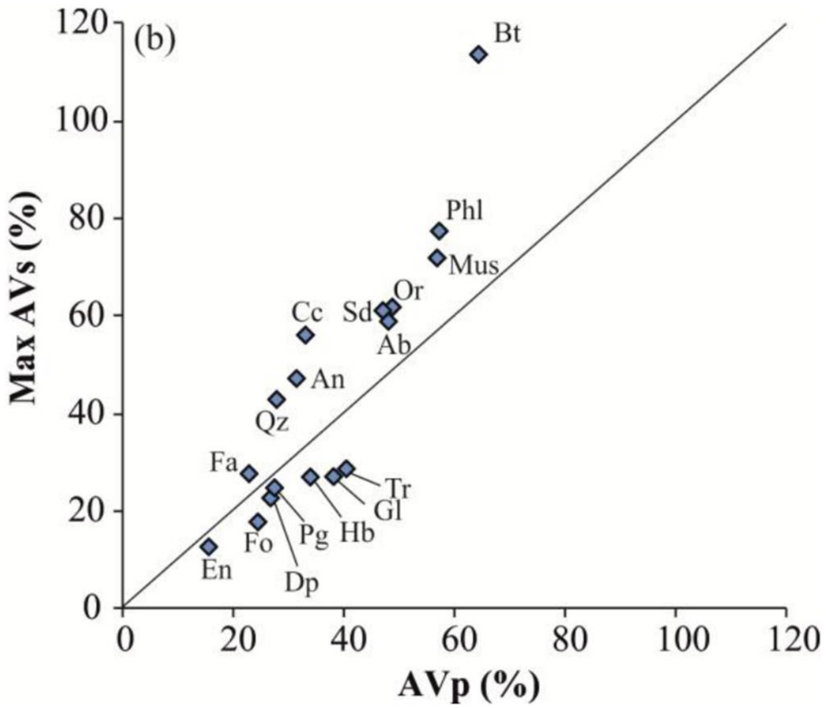

Figure 21. Plot of Vp anisotropy (AVp) and maximum Vs anisotropy (AVs) for some crustal minerals. Voigt-Reuss- Hill averaging (Almqvist and Mainprice, 2017) was used to calculate anisotropy. Mineral abbreviations are, albite (Ab), Anorthite (An), biotite (Bt), calcite (Cc), diopside (Dp), enstatite (En), fayalite (Fa), forsterite (Fo), hornblende (Hb), glaucophane (Gl), muscovite (Mus), orthoclase (Or), quartz (Qz), pargasite (Pg), phlogopite (Phl), richterite (Ri), sanidine (Sd), tremolite (Tr). Figure from Almqvist and Mainprice, (2017).

6.2 Anisotropy and Vs structure of the RMCC

Strain localization is essential to MCC formation (Block and Royden., 1990; Lavier et al., 1999; Rey et al., 2009). This observation partly motivated this research as radial anisotropy can be a proxy for strain. However, our radial anisotropy results are not closely correlated with the RMCC along its entire length. Maps (Fig. 16) and cross sections (Fig. 18,19) of anisotropy using varying models of crustal thickness as well as mean NBR and RMCC profiles of anisotropy as a function of depth (Fig. 20) show that clear comparisons of anisotropic pattern and RMCC structure cannot be confidently made because stronger than average radial anisotropy is found beneath the southern RMCC while weaker than average anisotropy is found beneath the northern RMCC. Furthermore, radial anisotropy results using RMSE crustal thicknesses that consider a crustal welt (Litherland and Klemperer, 2017; Fig. 19) closely resemble patterns of radial anisotropy using the three other crustal thickness models and do not deviate enough to be interpretable as a unique anisotropic pattern below the RMCC.

This lack of correlation indicates that the RMCC plays a nominal role in controlling the anisotropy presently observed lending to three possibilities: (1) mechanisms of core complex exhumation never produced a resolvable radial anisotropy pattern; (2) anisotropy associated with RMCC exhumation has subsequently been overprinted; or (3) radial anisotropy methods of this paper are not sensitive to or cannot resolve complex geometries of anisotropy (i.e. ~45° shear zone).

One example of the third possibility is the limited period range of surface wave dispersion (5-40 s Rayleigh and 6-40 s Love) used to resolve uppermost crust structures.

However, sensitivity kernels (Fig. 6) indicate our period range is, at least partly, sensitive to structure in the upper crust. This is supported by observations of high interstation phase velocities (Fig. 9) and high Vs (Fig. 15) directly below the RMCC in the upper crust. Furthermore, considering the RMCC has been exhumed from deep to middle crustal depths, we expect to see remnants of such strains much deeper than the shallow crust. Thus, we consider both 1 and 2 viable options and consequently specific models of RMCC exhumation are not further discussed. Similarities in magnitude and depth distribution of anisotropy between the RMCC and NBR (Fig. 20) suggest that any discussion should unify anisotropy sources for the RMCC and NBR. In the following section we explore the possibilities of a regional NBR fabric sourced from SPO and LPO fabrics and the possible overprinting of RMCC exhumation structures by post Miocene extension.

6.3 Regional NBR mid-crustal anisotropic signal

To first order our results agree with results from radial anisotropy studies of the Basin and Range (Moschetti et al., 2010). In fact, using similar prior constraints including forced isotropy in the upper crust and a monotonic increase of Vs, within our inversion approximately reproduces results by Moschetti et al., (2010) (Fig. 22). Aside from increased spatial resolution the inversion approach used here improves upon the inversion used by Moschetti et al., (2010) in a few ways. First, rather than using a single layered starting model in the crust the BMMC inversion does not require an initial starting model but rather a defined model space range that is then objectively interrogated. Second, we use the posterior distributions from the BMMC inversion to statistically asses where anisotropy is needed. From a depth dependent perspective our results improve upon Moschetti et al., (2010) and suggest that the role of positive radial anisotropy below and surrounding the RMCC is much larger in the middle crust than in the lower crust.

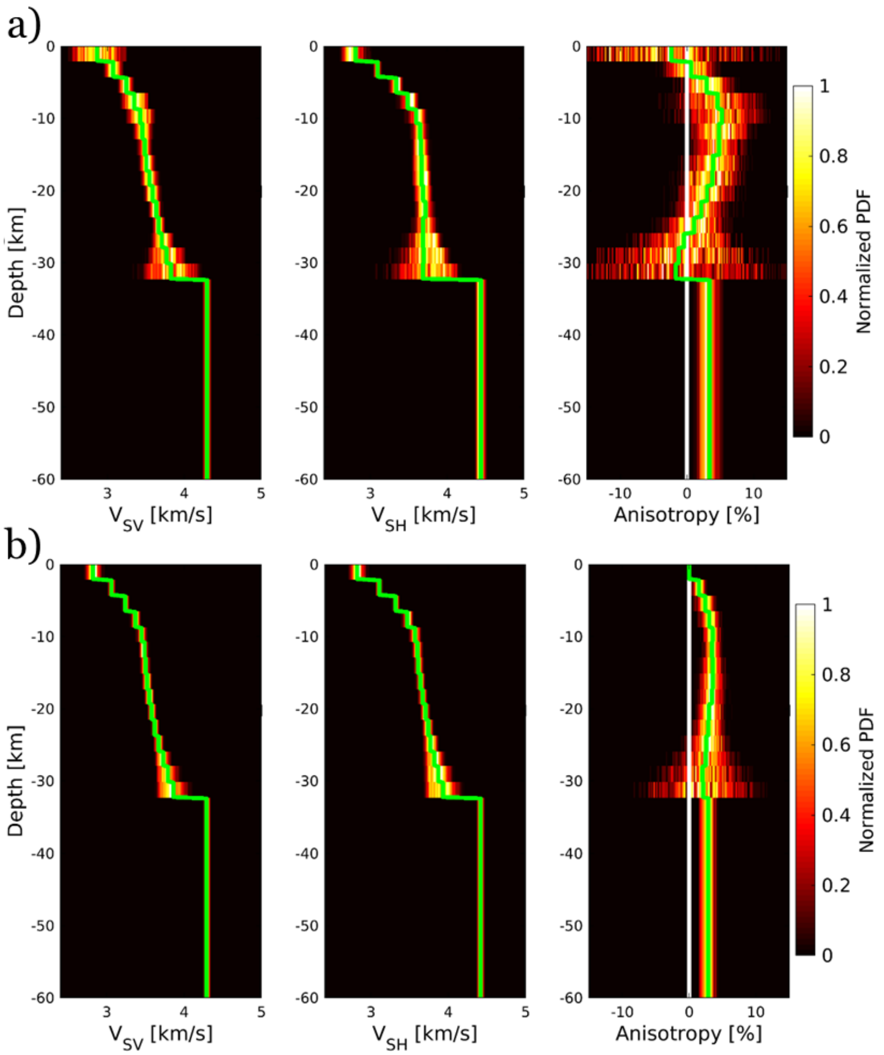

Figure 22. Posterior probability distribution as a function of depth for V_{SV}, V_{SH}, and anisotropy showing re-creation of Moschetti et al., (2010) results using piercing point 40°, -116°, a point also used to demonstrate results by Moschetti et al., (2010). Green line is the mean of the posterior distribution. a) Anisotropic BMMC inversion results with parameterizations and constraints from this study. b) Anisotropic BMMC inversion results with forced isotropy in the upper crust and a forced increase in velocity with increasing depth, constraints implemented by Moschetti et al., (2010). Notice anisotropy appears more reliable and is distributed fairly evenly in the middle and lower crust.

Modeling of extension suggests that on geologic timescales both the middle and lower crust can flow (Gans, 1987; Mckenzie et al., 2000). Invoking such flow Moschetti et al., (2010), hypothesized their observed 3.6 % mean positive radial anisotropy in the middle and lower crust of the NBR was sourced from LPO of mica and amphibole. This interpretation could explain our observations. However, large uncertainties in such interpretations remain. For example, a change in bulk rock symmetry systems could affect this interpretation. Furthermore, rheological and petrologic conditions and the potential depth variations of their associated boundaries may play a significant role in controlling crustal anisotropy. One rheological condition dependent boundary is the brittle - ductile transition (BDT).

The distribution of strength in the crust and BDT location at depth depends on tectonic setting, water content, strain rate, crustal thickness and composition, and temperature (Condie, 2015). Assuming heat flow of 50 mW/m^2 the BDT will occur at depths ~15 - 20 km (Condie, 2015). The Basin and Range is a region of high heat flow (Blackwell et al., 2011). As mentioned earlier the Basin and Range has a median heat flow of 79 mW/m^2 (Hasterok and Chapman, 2007) which would have the effect of placing the BDT much shallower. Under numerous assumptions Cooper et al., (2017) invoke a ~12 km BDT that corresponds to ~300° C. However, Basin and Range BDT depths can be as shallow as ~8 km (Lerch et al., 2010; Smith and Bruhn, 1984).

Below the BDT rocks have the capacity to flow. This flow has potential to create significant layering due to gneissic and/or migmatitic banding thus contributing to SPO fabric. Simultaneously, this flow has the potential to preferentially orient anisotropic minerals such as mica and amphibole within rocks to create a coherent and resolvable LPO signal. Consequently, it is possible that LPO and SPO are actually endmember anisotropic mechanisms and that our observed middle crustal radial anisotropy results include some component of both. Additionally, it is possible that some combination of rheologic and petrologic conditions are responsible for controlling the middle crust, upper (~5 km) and lower (~20 km), depth dependency bounds of our observed radial anisotropy results. Considering all such options results in a number of valid interpretations for both SPO and LPO sourced anisotropy. Here we discuss a few.

6.3.1 Possible SPO sources

Studying rocks from three Basin and Range MCC, including the RMCC, Cooper et al., (2017) identified two rheologic boundaries, the BDT (~12 km) and a deeper localized-distributed transition (LDT) (~20 km). It is thought that the lower crust is mainly metamorphic rocks in the granulite facies (Rudnick and Fountain, 1995). One interpretation of our results suggests the upper bound of anisotropy (~5 km) is controlled by the BDT beneath which flow can induce gneissic or migmatitic compositional layering and the lower bound of anisotropy (~20 km) is controlled by the LDT beneath which strain is diffusely distributed throughout more equant grains in the granulite facies. Our observed upper bound of anisotropy is shallower than inferred BDT depths of 8-12 km (Cooper et al., 2017; Lerch et al., 2010; Smith and Bruhn, 1984), but it is possible that this reflects preservation of anisotropy generated beneath the BDT and then exhumed to shallower depths.

Results from recent radial anisotropy studies below silicic caldera-forming volcanos resolved positive radial anisotropy in the middle (Jaxybulatov et al., 2014; Jiang et al., 2018) crust attributed to SPO from sill like magma reservoir structure. Jiang et al., (2018), using the same inversion methodology as we use here, isolate a positive radial anisotropy signal directly below the current location of the Yellowstone hotspot. No significant anisotropy is observed below the older Heise and Picabo volcanic fields on the Yellowstone hotspot track indicating anisotropy is actively evolving and not frozen in at those locations. One of the most voluminous silicic volcanic events in the geologic record (Best et al., 2009), known as the ignimbrite flare up, transpired within the same area as, but just before (Eocene to Miocene), the initiation of the modern Basin and Range. Numerous (>20) calderas (Best et al., 2016) existed and erupted in the Basin and Range during this time.

Possible frozen in sill like crustal structures serving as magma reservoirs for these calderas responsible for the ignimbrite flare up could form an SPO fabric (Fig. 7) and produce a positive middle crust anisotropic signal. Whether the calderas that participated in the ignimbrite flare up could create such a large and extensive amalgamated positive radial anisotropy signal remains unknown. Even if they could a few issues arise with this hypothesis. First, almost all of the >20 calderas responsible for the ignimbrite flare up are located south of or study region (Best et al., 2016). Second, strain associated with the extension of the Basin and Range may of overprinted or dissected any associated sill like structures. Lastly, recent studies suggest sill like structures associated with calderas may not be preserved at all, or at least do not produce a resolvable radial anisotropy signal (Jiang et al., 2018).

6.3.2 Possible LPO sources

As discussed earlier the interpretations of Moschetti et al., (2010) remain a valid explanation of our results. Mechanisms of deformation like dislocation and diffusion creep are outside of the scope of this research. However, deformation or flow is required for anisotropic minerals to become preferentially oriented and produce a resolvable anisotropic signal. Thus, even in an LPO interpretation the BDT can be invoked as a control on the anisotropic signal. The capacity to accurately identify the roles of certain crustal minerals in anisotropy investigations is in its infancy. Regardless, mica is a prime source candidate. It is possible that the abundance of mica in the middle crust (Almqvist and Mainprice, 2017) in conjunction with Basin and Range extensional strain is contributing to an LPO fabric and producing the observed regional mid-crustal anisotropic signal. The high heat flow of the Basin and Range might be creating a shallowly dipping geothermal gradient creating P-T conditions where mica becomes unstable at lower crustal depths and is lost. However, Hacker et al., (2014) argue that wholesale breakdown of mica is not necessary at high P-T conditions. Loss of mica due to P-T conditions invokes a petrologic control on the lower depth bound of our observed anisotropy. Both rheology and petrology are strongly temperature dependent and are therefore intrinsically linked. Again, it is also possible that that both rheologic (localized-distributed strain) and petrologic (removal of mica due to P-T condition) boundaries are coincident at a given depth and mutually control the lower depth bound of anisotropy.

Based on the relative flatness of the Moho throughout the Basin and Range It has been proposed that the majority of the current Moho below the Basin and Range is a product of extension (Klemperer et al., 1986). If true, this means that the Basin and Range Moho is younger than Miocene. If deformation was of the magnitude that the paleo-Moho was altered to the modern Moho it is not too big a leap to deduce that the middle, and at the very least the lower crust, below the RMCC either participated or were affected. Consequently, if the deep crust was flowing to accommodate extension during this period, it is reasonable to consider emplacement of a regional LPO flow fabric and overprinting of any possible anisotropy producing fabrics associated with RMCC exhumation.

6.4 Comparison with other tectonic settings

Radial anisotropy studies conducted in various tectonic settings at different geographic locations appear to have much more complex patterns of anisotropy (Das and Rai, 2017; Dreiling et al., 2017; Fu and Li, 2015; Lynner et al., 2018; Ojo et al., 2017). We think these differences might arise from: (1) local complexity of geologic structure; (2) differences in inversion techniques and parameterizations; and/or (3) representation of radial anisotropy without statistical discrimination. This study adopts methods put forth by Shen et al., (2012) and Xie et al., (2013) which we feel more accurately constrains radial anisotropy. Thus, our result of ~6% positive ($V_{SH} > V_{SV}$) anisotropy signal distributed throughout the middle crust (~5-20 km) required at 95% (Fig. 23) is more analogous to results from Xie et al., (2013) and Jiang et al., (2018) who used similar methods and also found positive radial anisotropy at mid-crustal depths. Another study conducted in the Songliao Basin, China which has a similar tectonic history to the Basin and Range, compression and shortening immediately followed by extension and MCC formation (Meng, 2003; Meng et al., 2003), used a similar BMMC Vs inversion technique and obtained results similar to ours (Guo et al, 2016).

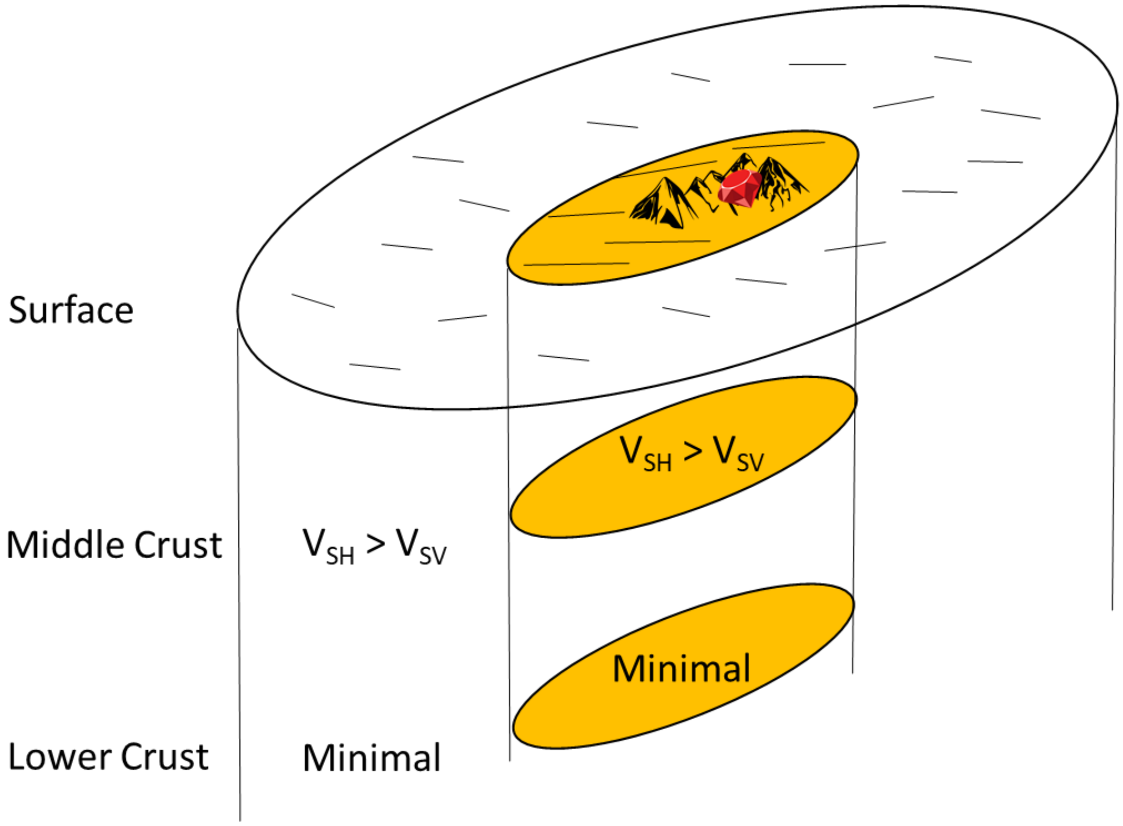

Figure 23. Cartoon of key results. Short lines represent deformation evident at the surface and the length of lines represent magnitude of deformation.

7 CONCLUSION

The BMMC inversion method used here improves upon linear inversion methods of previous regional Basin and Range radial anisotropy studies allowing for detailed analysis of anisotropy as a function of depth and statistical determination of where anisotropy is necessary. Our radial anisotropy results show a pervasive, ~6%, positive ($V_{SH} > V_{SV}$) signal distributed throughout the middle crust (~5-20 km) is required at 95% confidence. This result improves upon previous regional Basin and Range anisotropy studies in that radial anisotropy is insignificant in the lowermost crust. Variations in crustal thickness do not strongly influence these results. Although our results image the high Vs metamorphic core of the RMCC in the upper crust, we see no distinctive signature of anisotropy indicating mechanisms of core complex exhumation either never produced a resolvable radial anisotropy pattern or anisotropy associated with RMCC exhumation has subsequently been overprinted. If an interpretation of RMCC overprinting by a regional mechanism is correct then we would expect this pattern of anisotropy to persist throughout the majority of the Basin and Range and below other MCC of the Basin and Range, namely the Snake Range. Although results from this research can be explained by previous regional interpretations that invoke a LPO fabric produced by deep crustal flow orienting anisotropic minerals, multiple interpretations including SPO fabrics that invoke rheologically controlled boundaries remain valid possibilities. Furthermore, it is possible that SPO and LPO fabrics and rheologic and petrologic controls on these fabrics act as endmembers mutually contributing to the observed depth dependency and horizontal distribution of our anisotropy results.

Additional joint geophysical and geologic research could aid in illuminating the full importance of our results through accurate identification of controls on and implications of crustal anisotropy below MCC and the NBR.

REFERENCES

Aki, K. (1957), Space and time spectra of stationary stochastic waves, with special reference to microtremors, Bull.Earth.Res.Inst., 35, 415-456.

Aki, K. (1965), A note on the use of microseisms in determining the shallow structures of the earth's crust, Geophysics, 30(4), 665-666.

Almqvist, B. S. and D. Mainprice (2017), Seismic properties and anisotropy of the continental crust: Predictions based on mineral texture and rock microstructure, Rev. Geophys., 55(2), 367-433.

Armstrong, R. L. (1982), Cordilleran metamorphic core complexes--From Arizona to southern Canada, Annu. Rev. Earth Planet. Sci., 10(1), 129-154.

Babuska, V. and M. Cara (1991), Seismic anisotropy in the Earth, vol. 10, Springer Science & Business Media.

Backus, G. E. (1962), Long-wave elastic anisotropy produced by horizontal layering, Journal of Geophysical Research, 67(11), 4427-4440.

Bensen, G., M. Ritzwoller, M. Barmin, A. Levshin, F. Lin, M. Moschetti, N. Shapiro, and Y. Yang (2007), Processing seismic ambient noise data to obtain reliable broad-band surface wave dispersion measurements, Geophysical Journal International, 169(3), 1239-1260.

Best, M. G., D. L. Barr, E. H. Christiansen, S. Gromme, A. L. Deino, and D. G. Tingey (2009), The Great Basin Altiplano during the middle Cenozoic ignimbrite flareup: Insights from volcanic rocks, Int. Geol. Rev., 51(7-8), 589-633.

Best, M. G., E. H. Christiansen, S. de Silva, and P. W. Lipman (2016), Slab-rollback ignimbrite flareups in the southern Great Basin and other Cenozoic American arcs: A distinct style of arc volcanism, Geosphere, 12(4), 1097-1135.

Blackwell, D., M. Richards, Z. Frone, A. Ruzo, R. Dingwall, and M. Williams (2011), Temperature-At-Depth Maps for the Conterminous US and Geothermal Resource Estimates, GRC Transactions, 35(GRC1029452).

Block, L. and L. H. Royden (1990), Core complex geometries and regional scale flow in the lower crust, Tectonics, 9(4), 557-567.

Brownlee, S. J., V. Schulte-Pelkum, A. Raju, K. Mahan, C. Condit, and O. F. Orlandini (2017), Characteristics of deep crustal seismic anisotropy from a compilation of rock elasticity tensors and their expression in receiver functions, Tectonics, 36(9), 1835-1857.

Buck, W. R. (1988), Flexural rotation of normal faults, Tectonics, 7(5), 959-973.

Camp, V. E., K. L. Pierce, and L. A. Morgan (2015), Yellowstone plume trigger for Basin and Range extension, and coeval emplacement of the Nevada–Columbia Basin magmatic belt, Geosphere, 11(2), 203-225.

Christensen, N. I. and W. D. Mooney (1995), Seismic velocity structure and composition of the continental crust: A global view, Journal of Geophysical Research: Solid Earth, 100(B6), 9761-9788.

Colgan, J. P., K. A. Howard, R. J. Fleck, and J. L. Wooden (2010), Rapid middle Miocene extension and unroofing of the southern Ruby Mountains, Nevada, Tectonics, 29(6).

Condie, K. C. (2015), Earth as an evolving planetary system, Academic Press.

Coney, P. J. and T. A. Harms (1984), Cordilleran metamorphic core complexes: Cenozoic extensional relics of Mesozoic compression, Geology, 12(9), 550-554.

Coney, P. (1987), The regional tectonic setting and possible causes of Cenozoic extension in the North American Cordillera, Geological Society, London, Special Publications, 28(1), 177-186.

Cooper, F. J., J. P. Platt, and W. M. Behr (2017), Rheological transitions in the middle crust: insights from Cordilleran metamorphic core complexes, Solid Earth, 8(1), 199.

Crafford, A. E. J. (2007), Geologic map of Nevada, Citeseer.

Das, R. and S. Rai (2017), Extensive seismic anisotropy in the lower crust of Archean metamorphic terrain, South India, inferred from ambient noise tomography, Tectonophysics, 694, 164-180.

Davis, G. H. and P. J. Coney (1979), Geologic development of the Cordilleran metamorphic core complexes, Geology, 7(3), 120-124.

DeCelles, P. G. (2004), Late Jurassic to Eocene evolution of the Cordilleran thrust belt and foreland basin system, western USA, Am. J. Sci., 304(2), 105-168.

Dokka, R. K., M. J. Mahaffie, and A. W. Snoke (1986), Thermochronologic evidence of major tectonic denudation associated with detachment faulting, Northern Ruby Mountains-East Humboldt Range, Nevada, Tectonics, 5(7), 995-1006.

Dreiling, J., F. Tilmann, X. Yuan, J. Giese, E. Rindraharisaona, G. Rümpker, and M. Wysession, Crustal radial anisotropy and linkage to geodynamic processes–a study based on seismic ambient noise in southern Madagascar, Journal of Geophysical Research: Solid Earth.

Dziewonski, A., S. Bloch, and M. Landisman (1969), A technique for the analysis of transient seismic signals, Bulletin of the seismological Society of America, 59(1), 427-444.

Ekström, G. (2014), Love and Rayleigh phase-velocity maps, 5–40 s, of the western and central USA from USArray data, Earth Planet. Sci. Lett., 402, 42-49.

Erdman, M. E., B. R. Hacker, G. Zandt, and G. Seward (2013), Seismic anisotropy of the crust: electron-backscatter diffraction measurements from the Basin and Range, Geophysical Journal International, 195(2), 1211-1229.

Faulds, J. E. and R. J. Varga (1998), The role of accommodation zones and transfer zones in the regional segmentation of extended terranes, Geological Society of America Special Papers, 323, 1-45.

Fenneman, N. M. (1917), Physiographic Subdivision of the United States, Proc. Natl. Acad. Sci. U. S. A., 3(1), 17-22.

Fu, Y. V. and A. Li (2015), Crustal shear wave velocity and radial anisotropy beneath the Rio Grande rift from ambient noise tomography, Journal of Geophysical Research: Solid Earth, 120(2), 1005-1019.

Gans, P. B. (1987), An open-system, two-layer crustal stretching model for the Eastern Great Basin, Tectonics, 6(1), 1-12.

Guo, Z., Y. Yang, and Y. J. Chen (2016), Crustal radial anisotropy in Northeast China and its implications for the regional tectonic extension, Geophysical Journal International, 207(1), 197-208.

Hacker, B., M. Ritzwoller, and J. Xie (2014), Partially melted, mica-bearing crust in Central Tibet, Tectonics, 33(7), 1408-1424.

Haines, S. H. and van der Pluijm, Ben A (2010), Dating the detachment fault system of the Ruby Mountains, Nevada: Significance for the kinematics of low-angle normal faults, Tectonics, 29(4).

Hamilton, W. and W. B. Myers (1966), Cenozoic tectonics of the western United States, Rev. Geophys., 4(4), 509-549.

Hammond, W. C., G. Blewitt, and C. Kreemer (2014), Steady contemporary deformation of the central Basin and Range Province, western United States, Journal of Geophysical Research: Solid Earth, 119(6), 5235-5253.

Hammond, W. C. and W. Thatcher (2004), Contemporary tectonic deformation of the Basin and Range province, western United States: 10 years of observation with the Global Positioning System, Journal of Geophysical Research: Solid Earth, 109(B8).

Hammond, W. C. and W. Thatcher (2007), Crustal deformation across the Sierra Nevada, northern Walker Lane, Basin and Range transition, western United States measured with GPS, 2000–2004, Journal of Geophysical Research: Solid Earth, 112(B5).

Hansen, S. M., K. Dueker, and B. Schmandt (2015), Thermal classification of lithospheric discontinuities beneath USArray, Earth Planet. Sci. Lett., 431, 36-47.

Hasterok, D. and D. S. Chapman (2007), Continental thermal isostasy: 1. Methods and sensitivity, Journal of Geophysical Research: Solid Earth, 112(B6).

Hastings, W. K. (1970), Monte Carlo sampling methods using Markov chains and their applications, Biometrika, 57(1), 97-109.

Herrmann, R. B. (2013), Computer programs in seismology: An evolving tool for instruction and research, Seismol. Res. Lett., 84(6), 1081-1088.

Herrmann, R. B., H. Benz, and C. Ammon (2011), Monitoring the earthquake source process in North America, Bulletin of the Seismological Society of America, 101(6), 2609-2625.

Hess, H. (1964), Seismic anisotropy of the uppermost mantle under oceans, Nature, 203(4945), 629-631.

Hodges, K. and J. D. Walker (1990), Petrologic constraints on the unroofing history of the Funeral Mountain metamorphic core complex, California.

Hudec, M. R. (1992), Mesozoic structural and metamorphic history of the central Ruby Mountains metamorphic core complex, Nevada, Geological Society of America Bulletin, 104(9), 1086-1100.

Jaxybulatov, K., N. M. Shapiro, I. Koulakov, A. Mordret, M. Landes, and C. Sens-Schonfelder (2014), Volcanology. A large magmatic sill complex beneath the Toba caldera, Science, 346(6209), 617-619, doi:10.1126/science.1258582.

Jiang, C., B. Schmandt, J. Farrell, F. Lin, and K. M. Ward (2018), Seismically anisotropic magma reservoirs underlying silicic calderas, Geology, 46(8), 727-730.

Kistler, R., E. Ghent, and J. O'neil (1981), Petrogenesis of garnet two-mica granites in the Ruby Mountains, Nevada, Journal of Geophysical Research: Solid Earth, 86(B11), 10591-10606.

Klemperer, S. L., T. Hauge, E. Hauser, J. Oliver, and C. Potter (1986), The Moho in the northern Basin and Range province, Nevada, along the COCORP 40 N seismic-reflection transect, Geological Society of America Bulletin, 97(5), 603-618.

Kreemer, C., W. C. Hammond, G. Blewitt, A. A. Holland, and R. A. Bennett (2012), A geodetic strain rate model for the Pacific-North American plate boundary, western United States, paper presented at EGU General Assembly Conference Abstracts.

Lavier, L. L., W. Roger Buck, and A. N. Poliakov (1999), Self-consistent rolling-hinge model for the evolution of large-offset low-angle normal faults, Geology, 27(12), 1127-1130.

Lerch, D. W., S. L. Klemperer, A. E. Egger, J. P. Colgan, and E. L. Miller (2010), The northwestern margin of the Basin-and-Range Province, part 1: Reflection profiling of the moderate-angle (~ 30) Surprise Valley Fault, Tectonophysics, 488(1-4), 143-149.

Levander, A. and M. S. Miller (2012), Evolutionary aspects of lithosphere discontinuity structure in the western US, Geochem. Geophys. Geosyst., 13(7).

Lin, F., M. P. Moschetti, and M. H. Ritzwoller (2008), Surface wave tomography of the western United States from ambient seismic noise: Rayleigh and Love wave phase velocity maps, Geophysical Journal International, 173(1), 281-298.

Lin, F., M. H. Ritzwoller, Y. Yang, M. P. Moschetti, and M. J. Fouch (2011), Complex and variable crustal and uppermost mantle seismic anisotropy in the western United States, Nature Geoscience, 4(1), 55-61.

Lin, P. P., J. B. Gaherty, G. Jin, J. A. Collins, D. Lizarralde, R. L. Evans, and G. Hirth (2016), High-resolution seismic constraints on flow dynamics in the oceanic asthenosphere, Nature, 535(7613), 538.

Litherland, M. M. and S. L. Klemperer (2017), Crustal structure of the Ruby Mountains metamorphic core complex, Nevada, from passive seismic imaging, Geosphere, 13(5), 1506-1523.

Lobkis, O. I. and R. L. Weaver (2001), On the emergence of the Green’s function in the correlations of a diffuse field, J. Acoust. Soc. Am., 110(6), 3011-3017.

Long, M. D. and T. W. Becker (2010), Mantle dynamics and seismic anisotropy, Earth Planet. Sci. Lett., 297(3), 341-354.

Long, M. D. and P. G. Silver (2008), The subduction zone flow field from seismic anisotropy: a global view, Science, 319(5861), 315-318, doi:10.1126/science.1150809.

Lynner, C., S. L. Beck, G. Zandt, R. W. Porritt, F. Lin, and Z. C. Eilon (2018), Midcrustal Deformation in the Central Andes Constrained by Radial Anisotropy, Journal of Geophysical Research: Solid Earth.

MacCready, T., A. W. Snoke, J. E. Wright, and K. A. Howard (1997), Mid-crustal flow during Tertiary extension in the Ruby Mountains core complex, Nevada, Geological Society of America Bulletin, 109(12), 1576-1594.

Mahan, K. (2006), Retrograde mica in deep crustal granulites: Implications for crustal seismic anisotropy, Geophys. Res. Lett., 33(24).

Mainprice, D. and A. Nicolas (2013), Development of shape and lattice preferred orientations: application to the seismic anisotropy of the lower crust, Current Topics in Structural Geology, 175.

McGrew, A. J., M. T. Peters, and J. E. Wright (2000), Thermobarometric constraints on the tectonothermal evolution of the East Humboldt Range metamorphic core complex, Nevada, Geological Society of America Bulletin, 112(1), 45-60.

McKenzie, D., F. Nimmo, J. A. Jackson, P. Gans, and E. Miller (2000), Characteristics and consequences of flow in the lower crust, Journal of Geophysical Research: Solid Earth, 105(B5), 11029-11046.

Meng, Q. (2003), What drove late Mesozoic extension of the northern China–Mongolia tract? Tectonophysics, 369(3-4), 155-174.

Meng, Q., J. Hu, J. Jin, Y. Zhang, and D. Xu (2003), Tectonics of the late Mesozoic wide extensional basin system in the China–Mongolia border region, Basin Research, 15(3), 397-415.

Miller, E. L., T. A. Dumitru, R. W. Brown, and P. B. Gans (1999), Rapid Miocene slip on the Snake Range–Deep Creek range fault system, east-central Nevada, Geological Society of America Bulletin, 111(6), 886-905.

Moschetti, M., M. Ritzwoller, F. Lin, and Y. Yang (2010), Seismic evidence for widespread western-US deep-crustal deformation caused by extension, Nature, 464(7290), 885-889.

Mosegaard, K. and A. Tarantola (1995), Monte Carlo sampling of solutions to inverse problems, Journal of Geophysical Research: Solid Earth, 100(B7), 12431-12447.

Nesbitt, H. and G. Young (1984), Prediction of some weathering trends of plutonic and volcanic rocks based on thermodynamic and kinetic considerations, Geochim. Cosmochim. Acta, 48(7), 1523-1534.

Ojo, A. O., S. Ni, and Z. Li (2017), Crustal radial anisotropy beneath Cameroon from ambient noise tomography, Tectonophysics, 696, 37-51.

Pérouse, E. and B. P. Wernicke (2017), Spatiotemporal evolution of fault slip rates in deforming continents: The case of the Great Basin region, northern Basin and Range province, Geosphere, 13(1), 112-135.

Platt, J. P., W. M. Behr, and F. J. Cooper (2015), Metamorphic core complexes: windows into the mechanics and rheology of the crust, Journal of the Geological Society, 172(1), 9-27.

Porter, R., G. Zandt, and N. McQuarrie (2011), Pervasive lower-crustal seismic anisotropy in Southern California: Evidence for underplated schists and active tectonics, Lithosphere, 3(3), 201-220.

Rey, P., C. Teyssier, and D. Whitney (2009), The role of partial melting and extensional strain rates in the development of metamorphic core complexes, Tectonophysics, 477(3), 135-144.

Rudnick, R. L. and D. M. Fountain (1995), Nature and composition of the continental crust: a lower crustal perspective, Rev. Geophys., 33(3), 267-309.

Schellart, W. P., D. R. Stegman, R. J. Farrington, J. Freeman, and L. Moresi (2010), Cenozoic tectonics of western North America controlled by evolving width of Farallon slab, Science, 329(5989), 316-319, doi:10.1126/science.1190366.

Schmandt, B., F. Lin, and K. E. Karlstrom (2015), Distinct crustal isostasy trends east and west of the Rocky Mountain Front, Geophys. Res. Lett., 42(23).

Schutt, D. L., A. R. Lowry, and J. S. Buehler (2018), Moho temperature and mobility of lower crust in the western United States, Geology.

Seats, K. J., J. F. Lawrence, and G. A. Prieto (2012), Improved ambient noise correlation functions using Welch' s method, Geophysical Journal International, 188(2), 513-523.

Shapiro, N. M., M. Campillo, L. Stehly, and M. H. Ritzwoller (2005), High-resolution surface-wave tomography from ambient seismic noise, Science, 307(5715), 1615-1618, doi:307/5715/1615.

Shapiro, N. M., M. H. Ritzwoller, P. Molnar, and V. Levin (2004), Thinning and flow of Tibetan crust constrained by seismic anisotropy, Science, 305(5681), 233-236, doi:10.1126/science.1098276.

Shearer, P. M. (2009), Introduction to seismology, Cambridge University Press.

Shen, W. and M. H. Ritzwoller (2016), Crustal and uppermost mantle structure beneath the United States, Journal of Geophysical Research: Solid Earth, 121(6), 4306-4342.

Shen, W., M. H. Ritzwoller, V. Schulte-Pelkum, and F. Lin (2012), Joint inversion of surface wave dispersion and receiver functions: a Bayesian Monte-Carlo approach, Geophysical Journal International, 192(2), 807-836.

Smith, R. B. and R. L. Bruhn (1984), Intraplate extensional tectonics of the eastern Basin-Range: Inferences on structural style from seismic reflection data, regional tectonics, and thermal-mechanical models of brittle-ductile deformation, Journal of Geophysical Research: Solid Earth, 89(B7), 5733-5762.

Stewart, J. H. and J. Faulds (1998), Regional characteristics, tilt domains, and extensional history of the late Cenozoic Basin and Range province, western North America, SPECIAL PAPERS-GEOLOGICAL SOCIETY OF AMERICA, 47-74.

Sullivan, W. A. and A. W. Snoke (2007), Comparative anatomy of core-complex development in the northeastern Great Basin, USA, Rocky Mountain Geology, 42(1), 1-29.

Unites States Geologic Survey, 2018: Quaternary Fault and Fold Database of the United States. [Available online at https://earthquake.usgs.gov/cfusion/qfault/show_report_AB.cfm?fault_id=1573&section_id=].

Ward, D., K. Mahan, and V. Schulte-Pelkum (2012), Roles of quartz and mica in seismic anisotropy of mylonites, Geophysical Journal International, 190(2), 1123-1134.

Wernicke, B. (1981), Low-angle normal faults in the Basin and Range Province: nappe tectonics in an extending orogen, Nature, 291, 645-648.

Wernicke, B., J. E. Spencer, B. C. Burchfiel, and P. L. Guth (1982), Magnitude of crustal extension in the southern Great Basin, Geology, 10(10), 499-502.

Wright, J. E. and A. W. Snoke (1993), Tertiary magmatism and mylonitization in the Ruby-East Humboldt metamorphic core complex, northeastern Nevada: U-Pb geochronology and Sr, Nd, and Pb isotope geochemistry, Geological Society of America Bulletin, 105(7), 935-952.

Xie, J., M. H. Ritzwoller, S. Brownlee, and B. Hacker (2015), Inferring the oriented elastic tensor from surface wave observations: preliminary application across the western United States, Geophysical Journal International, 201(2), 996-1021.

Xie, J., M. H. Ritzwoller, W. Shen, and W. Wang (2017), Crustal anisotropy across eastern Tibet and surroundings modeled as a depth-dependent tilted hexagonally symmetric medium, Geophysical Journal International, 209(1), 466-491.

Xie, J., M. H. Ritzwoller, W. Shen, Y. Yang, Y. Zheng, and L. Zhou (2013), Crustal radial anisotropy across eastern Tibet and the western Yangtze craton, Journal of Geophysical Research: Solid Earth, 118(8), 4226-4252.

Zandt, G., S. C. Myers, and T. C. Wallace (1995), Crust and mantle structure across the Basin and Range-Colorado Plateau boundary at 37 N latitude and implications for Cenozoic extensional mechanism, Journal of Geophysical Research: Solid Earth, 100(B6), 10529-10548.

SUPPLEMENTARY FIGURES

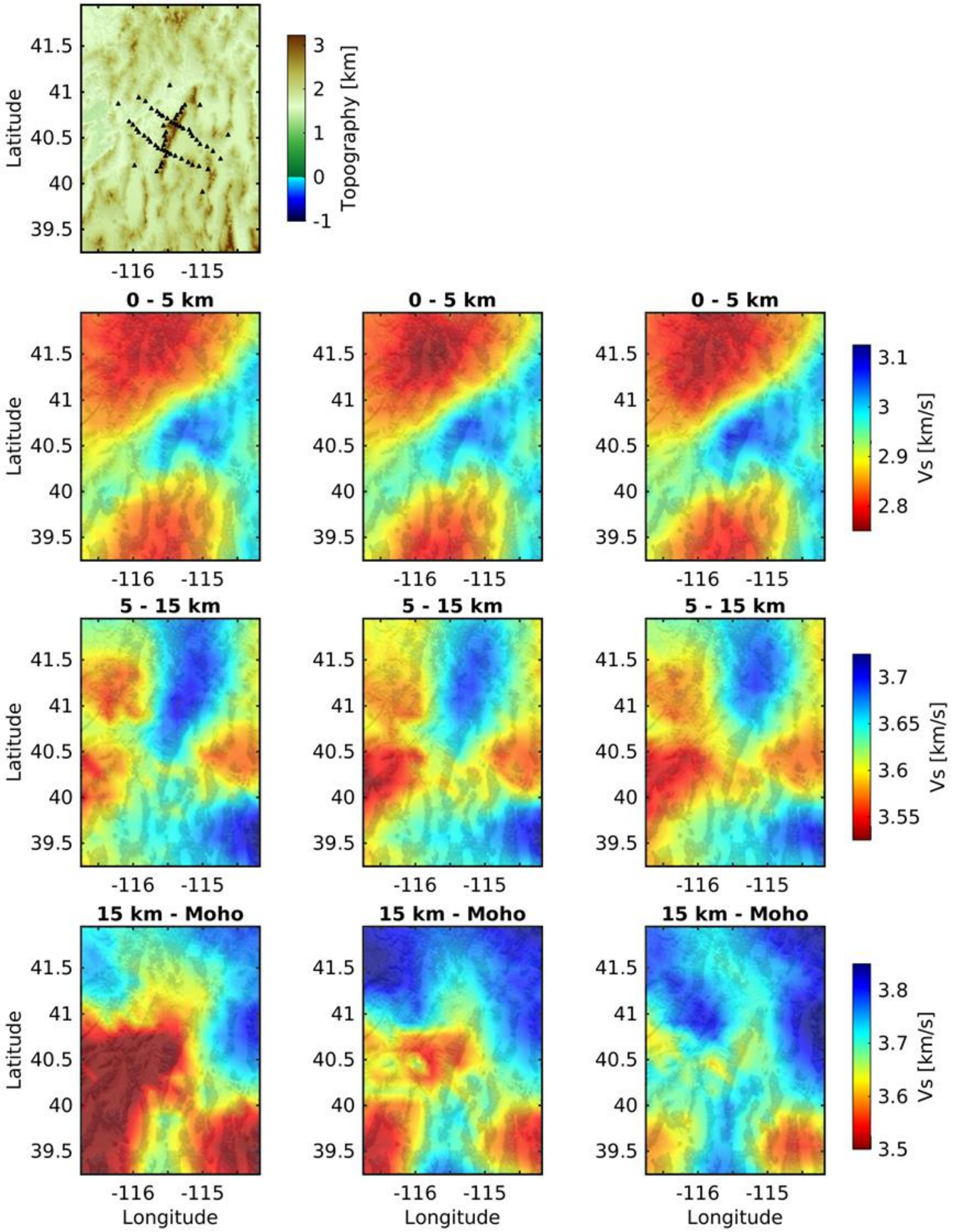

Supplementary Figure 1. Upper (0-5 km), middle (5-15 km), and lower (15 km - Moho) crustal depth averaged Isotropic Vs maps from isotropic BMMC inversions using crustal thickness models from A) Schutt et al., (2018) B) Schmandt et al., (2015) and C) Shen and Ritzwoller, (2016). Notice color bar range is different than in figure 15 and that middle crust velocities are, on average, faster.

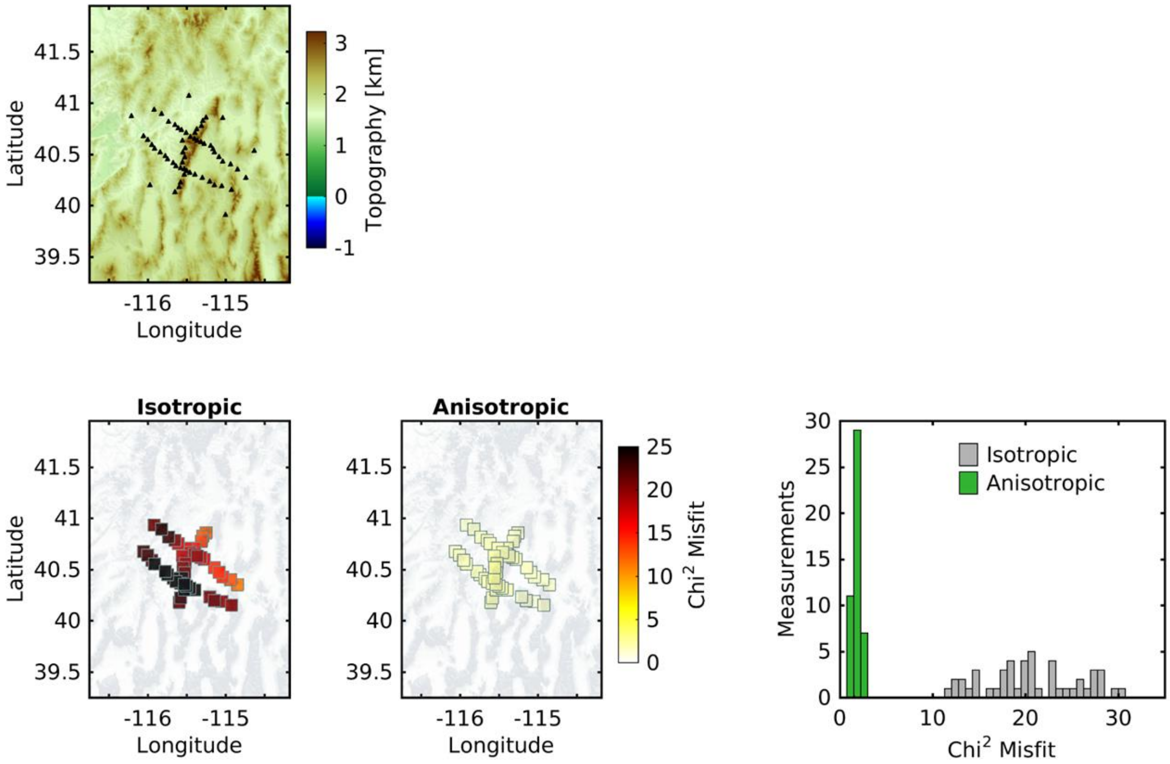

Supplementary Figure 2. Isotropic and anisotropic chi^2 misfit maps for crustal thicknesses below each of the RMSE stations from Litherland et al., (2018). Right column shows histograms of isotropic and anisotropic chi^2 misfit values.

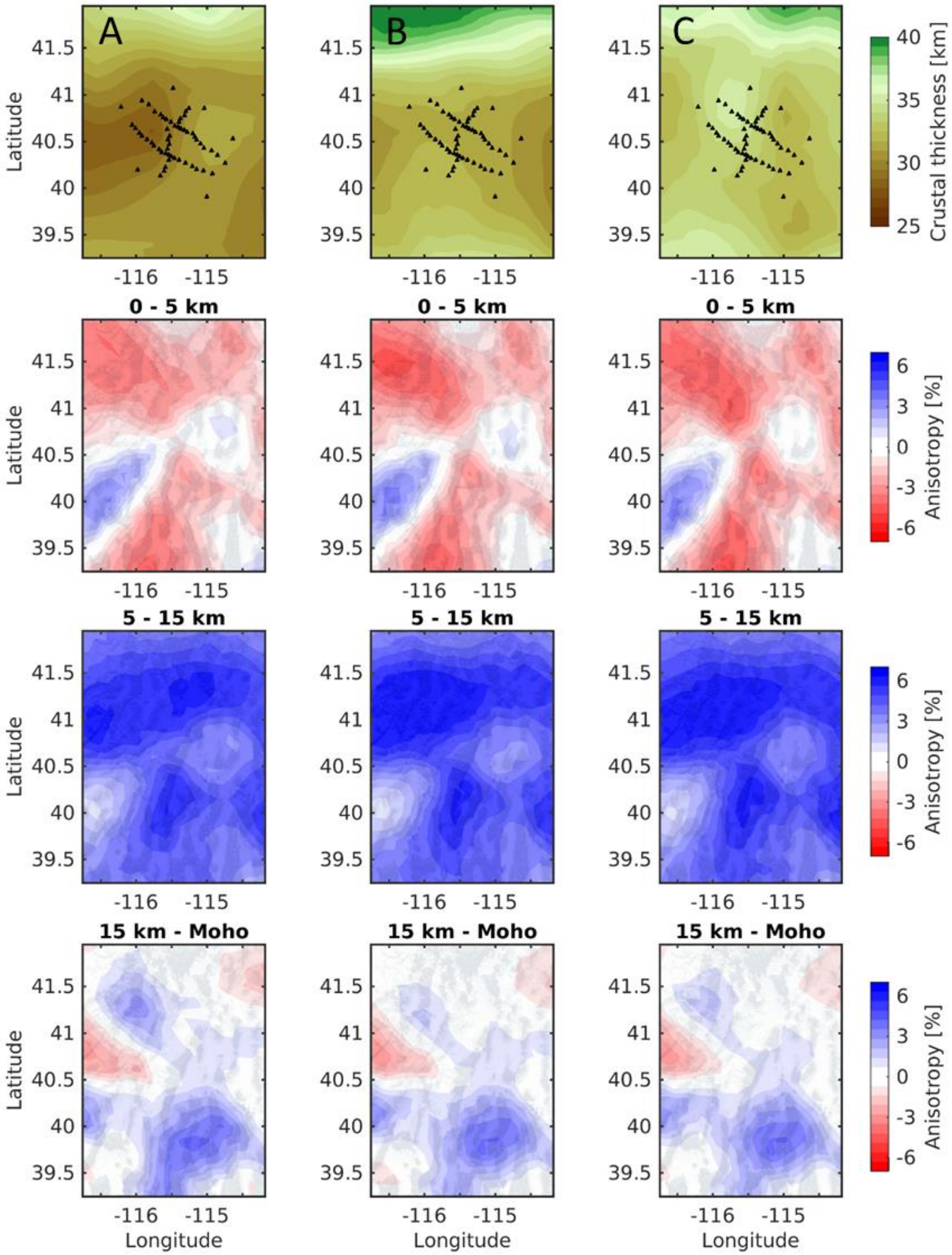

Supplementary Figure 3. Same as figure 16 but with no quality control implementation. Upper (0-5 km), middle (5-15 km), and lower (15 km - Moho) crustal depth averaged anisotropy maps from BMMC inversions using crustal thickness models from A) Schutt et al., (2018) B) Schmandt et al., (2015) and C) Shen and Ritzwoller, (2016). Upper row are maps of each crustal thickness model. Black triangles are RMSE stations.

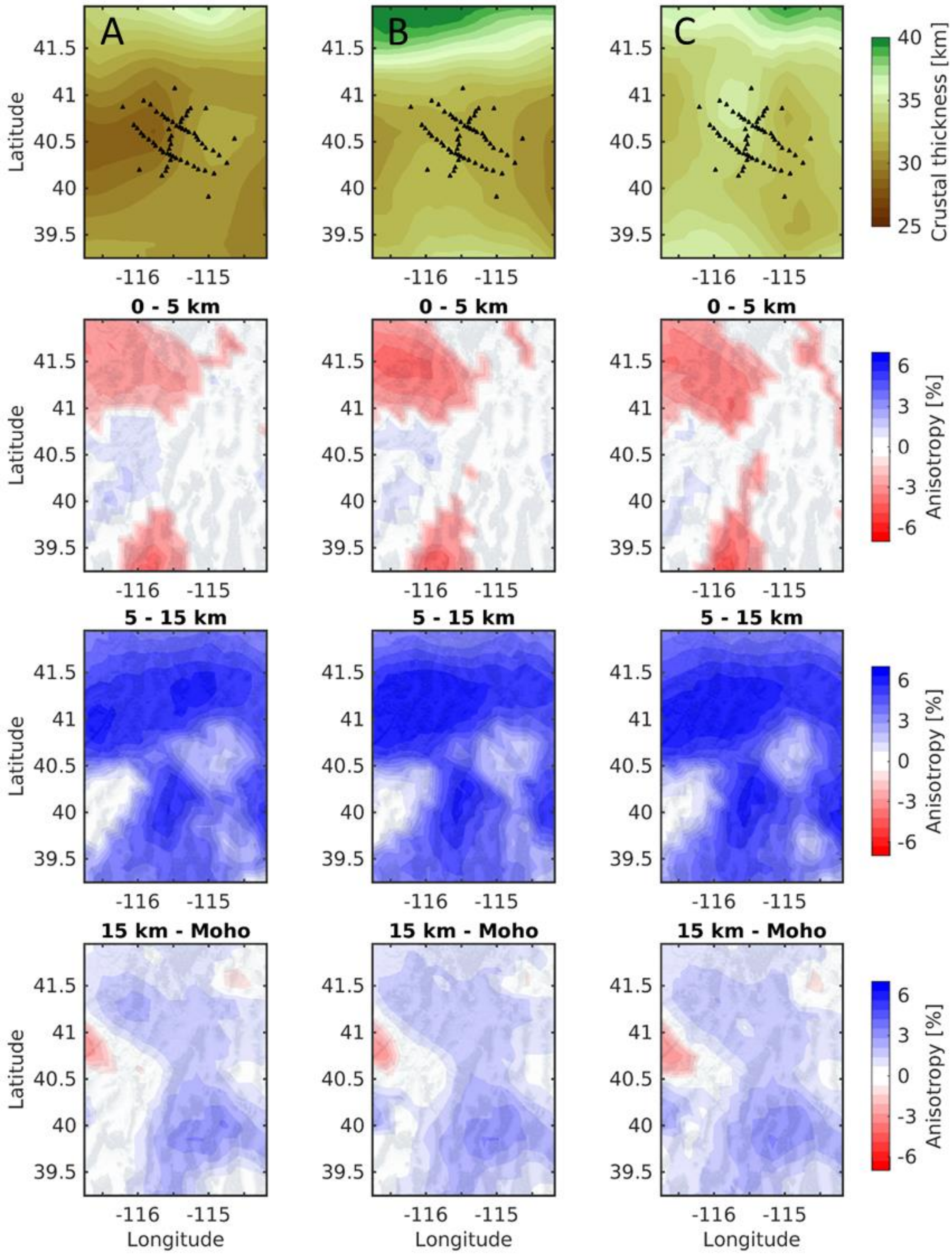

Supplementary Figure 4. Same as figure 16 but with only anisotropy that satisfies (|RA|-(σ))>0 plotted. Upper (0-5 km), middle (5-15 km), and lower (15 km - Moho) crustal depth averaged anisotropy maps from BMMC inversions using crustal thickness models from A) Schutt et al., (2018) B) Schmandt et al., (2015) and C) Shen and Ritzwoller, (2016). Upper row are maps of each crustal thickness model. Black triangles are RMSE stations.

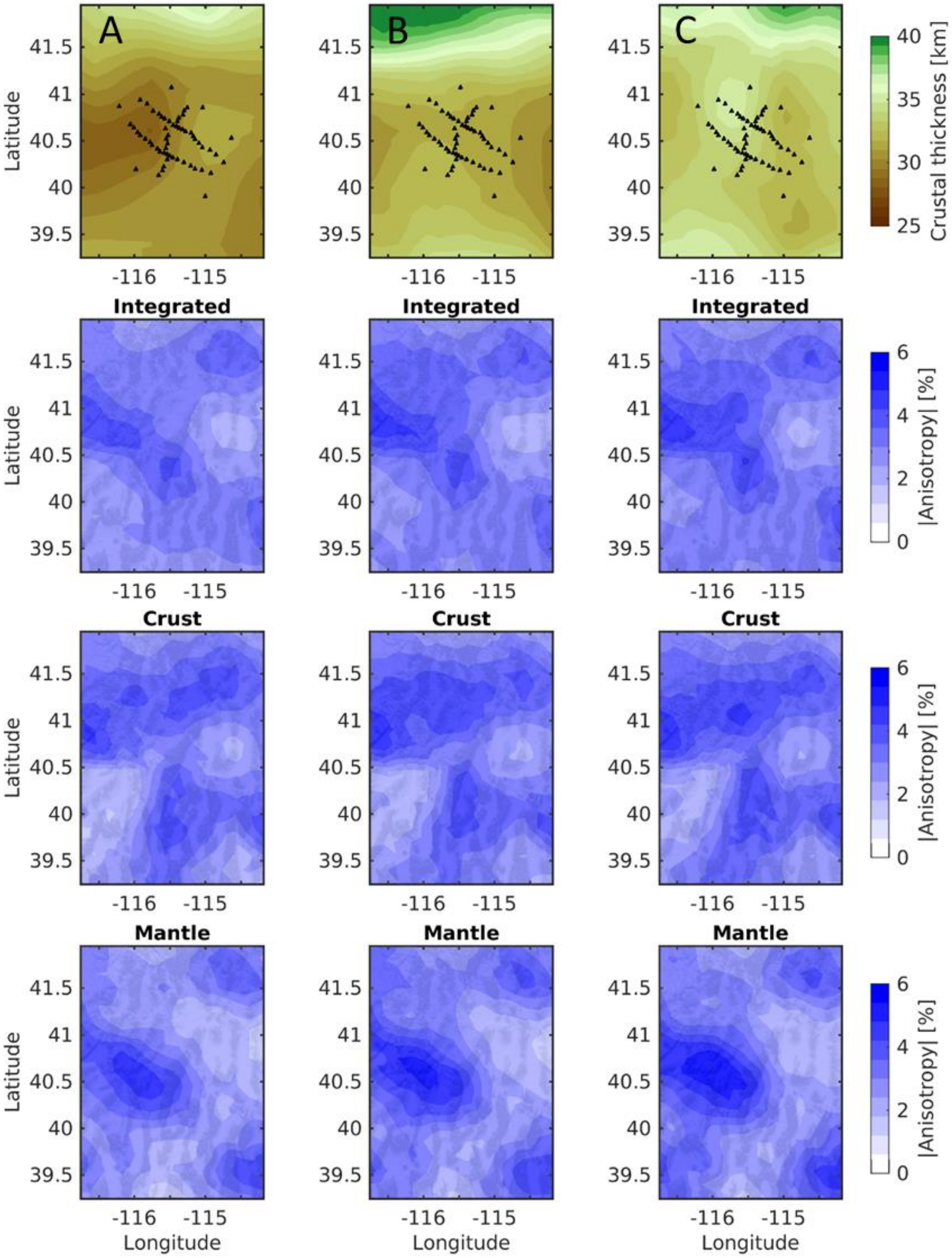

Supplementary Figure 5. Integrated (0-80 km), crust (0 km – Moho), and mantle (Moho – 80 km) depth averaged |RA| maps from BMMC inversions using crustal thickness models from A) Schutt et al., (2018) B) Schmandt et al., (2015) and C) Shen and Ritzwoller, (2016). Top row are maps of each of the crustal thickness models. RMSE stations (black triangles) serve as a spatial reference. High values in integrated |RA| maps correlate well with high chi^2 misfit trends in isotropic misfit maps (Fig. 14). Crust and mantle |RA| maps show areas in the crust and mantle that contribute to overall isotropic chi^2 misfit trend and where anisotropy is required. Notice trends in the crust and mantle |RA| maps are uncoupled.